Demonstrating the Use of Small Uncrewed Aircraft Systems (Drones) Capabilities and Data for Iowa Transportation and Infrastructure Work

Pilot Project No. 2 – Use of Small Uncrewed Aircraft Systems for Gravel Road Monitoring

Task Report | May 2026

IOWA STATE UNIVERSITY
Institute for Transportation

Sponsored by
Iowa Department of Transportation
and Federal Highway Administration
(SPR-RE24(010)-8H-00,
InTrans Project 24-904)

About the Program for Sustainable Pavement Engineering and Research

The overall goal of the Program for Sustainable Pavement Engineering and Research (PROSPER) is to advance research, education, and technology transfer in the area of sustainable highway and airport pavement infrastructure systems.

About the Institute for Transportation

The mission of the Institute for Transportation (InTrans) at Iowa State University is to save lives and improve economic vitality through discovery, research innovation, outreach, and the implementation of bold ideas.

Iowa State University Nondiscrimination Statement

Iowa State University does not discriminate on the basis of race, color, age, ethnicity, religion, national origin, pregnancy, sexual orientation, genetic information, sex, marital status, disability, or status as a U.S. Veteran. Inquiries regarding nondiscrimination policies may be directed to Office of Equal Opportunity, 2680 Beardshear Hall, 515 Morrill Road, Ames, Iowa 50011, telephone: 515-294-7612, email: eooffice@iastate.edu.

Disclaimer Notice

The contents of this report reflect the views of the authors, who are responsible for the facts and the accuracy of the information presented herein. The opinions, findings and conclusions expressed in this publication are those of the authors and not necessarily those of the sponsors.

The sponsors assume no liability for the contents or use of the information contained in this document. This report does not constitute a standard, specification, or regulation.

The sponsors do not endorse products or manufacturers. Trademarks or manufacturers' names appear in this report only because they are considered essential to the objective of the document.

Quality Assurance Statement

The Federal Highway Administration (FHWA) provides high-quality information to serve Government, industry, and the public in a manner that promotes public understanding. Standards and policies are used to ensure and maximize the quality, objectivity, utility, and integrity of its information. The FHWA periodically reviews quality issues and adjusts its programs and processes to ensure continuous quality improvement.

Iowa DOT Statements

The Iowa Department of Transportation (DOT) ensures non-discrimination in all programs and activities in accordance with Title VI of the Civil Rights Act of 1964. Any person who believes that they are being denied participation in a project, being denied benefits of a program, or otherwise being discriminated against because of race, color, national origin, gender, age, or disability, low income and limited English proficiency, or if needs more information or special assistance for persons with disabilities or limited English proficiency, please contact Iowa DOT Civil Rights at 515-239-7970 or by email at civil.rights@iowadot.us.

The preparation of this report was financed in part through funds provided by the Iowa DOT through its "Second Revised Agreement for Management of Research Conducted by Iowa State University for the Iowa Department of Transportation" and its amendments.

The opinions, findings, and conclusions expressed in this publication are those of the authors and not necessarily those of the Iowa DOT or the U.S. DOT FHWA.

Technical Report Documentation Page

1. Report No.	2. Government Accession No.	3. Recipient's Catalog No.
InTrans Project 24-904		

4. Title and Subtitle	5. Report Date
Demonstrating the Use of Small Uncrewed Aircraft Systems (Drones) Capabilities and Data for Iowa Transportation and Infrastructure Work: Pilot Project No. 2 – Use of Small Uncrewed Aircraft Systems for Gravel Road Monitoring	May 2026 6. Performing Organization Code

7. Author(s)	8. Performing Organization Report No.
Kunle S. Oguntoye (orcid.org/0009-0002-9993-3304), Md Abdullah All Sourav (orcid.org/0000-0003-3387-740X), Rajrup Mitra (orcid.org/0000-0003-1937-7222), Abby Jenkins (orcid.org/0009-0007-5860-421X), Halil Ceylan (orcid.org/0000-0003-1133-0366), Sunghwan Kim (orcid.org/0000-0002-1239-2350), Berk Gulmezoglu (orcid.org/0000-0001-6268-6325), Yunjeong (Leah) Mo (orcid.org/0000-0002-5162-2235) and Colin N. Brooks (orcid.org/0000-0003-4544-2569)	InTrans Project 24-904

9. Performing Organization Name and Address	10. Work Unit No. (TRAIS)
Program for Sustainable Pavement Engineering and Research (PROSPER) Institute for Transportation Iowa State University 2711 South Loop Drive, Suite 4700 Ames, IA 50010-8664	11. Contract or Grant No.

12. Sponsoring Organization Name and Address		13. Type of Report and Period Covered
Iowa Department of Transportation 800 Lincoln Way Ames, IA 50010	Federal Highway Administration 1200 New Jersey Avenue, SE Washington, DC 20590	Task Report 14. Sponsoring Agency Code SPR-RE24(010)-8H-00

15. Supplementary Notes

Visit https://prosper.intrans.iastate.edu/ for color pdfs of this and other research reports.

16. Abstract

According to the United States Department of Transportation (USDOT), gravel roads account for more than 30% of the total road network in the United States. Although these roads typically carry low volumes of traffic, they play a critical role in transporting goods, providing access to essential services, and connecting to larger highway systems. A 2012 USDOT study reported that gravel roads in Iowa make up 60% of the state's public road system, representing nearly 70,000 mi of roadways. Similar to paved roads, gravel roads are prone to various types of distress that, if not addressed promptly, can lead to cost-prohibitive maintenance and reconstruction. The sustainability of the overall health of these roads is crucial for ensuring smooth traffic flow and reducing traffic-related accidents.

Since the vast number of gravel roads and their remote locations make close monitoring a significant challenge, in this study, we explored the feasibility of adopting small uncrewed aircraft systems (sUAS) for remote sensing of gravel road networks. We also explored distress detection through the development of geographic information systems (GIS)-based proof-of-concept toolboxes that help quantify specific types of distress, including potholes, rutting, corrugation, loose aggregate, and improper crown (cross-section). In this experiment, we also considered methods for monitoring dust, a non-depth-based gravel road distress. Promising results from combining sUAS applications with the developed prototype toolboxes indicate that substantial time can be saved on gravel road inspections using the proposed workflow compared to traditional manual inspections. Moreover, based on the quantified distress data provided by the proposed workflow, county engineers and maintenance personnel will be better equipped to make informed decisions regarding maintenance needs.

17. Key Words	18. Distribution Statement
corrugation—crown—drones—drone for gravel road distress detection—dust—gravel road—infrastructure assessment—loose aggregate—pothole—rut—uncrewed (unmanned/unpersonned) aircraft systems	No restrictions.

19. Security Classification (of this report)	20. Security Classification (of this page)	21. No. of Pages	22. Price
Unclassified.	Unclassified.	63	NA

Form DOT F 1700.7 (8-72) **Reproduction of completed page authorized**

DEMONSTRATING THE USE OF SMALL UNCREWED AIRCRAFT SYSTEMS (DRONES) CAPABILITIES AND DATA FOR IOWA TRANSPORTATION AND INFRASTRUCTURE WORK

PILOT PROJECT NO. 2 - USE OF SMALL UNCREWED AIRCRAFT SYSTEMS FOR GRAVEL ROAD MONITORING

Pilot Project Report
May 2026

Principal Investigator
Halil Ceylan, Professor and Director
Program for Sustainable Pavement Engineering and Research (PROSPER),
Institute for Transportation, Iowa State University

Co-Principal Investigators
Sunghwan Kim, Research Scientist, Institute for Transportation, Iowa State University
Berk Gulmezoglu, Assistant Professor, Electrical and Computer Engineering, Iowa State University
Yunjeong (Leah) Mo, Assistant Professor, Civil, Construction and Environmental Engineering, Iowa State University
Colin N. Brooks, Transportation Practice Area Leader, Michigan Tech Research Institute (MTRI), Michigan Technological University

Research Associates
Md Abdullah All Sourav, Kunle Oguntoye, Rajrup Mitra, Abby Jenkins

Authors
Kunle S. Oguntoye, Md Abdullah All Sourav, Rajrup Mitra, Abby Jenkins, Halil Ceylan, Sunghwan Kim, Berk Gulmezoglu, Yunjeong (Leah) Mo, and Colin N. Brooks

Sponsored by
Iowa Department of Transportation and Federal Highway Administration
(SPR-RE24(010)-8H-00)

Preparation of this report was financed in part
through funds provided by the Iowa Department of Transportation
through its Research Management Agreement with the Institute for Transportation
(InTrans Project 24-904)

A report from
Program for Sustainable Pavement Engineering and Research (PROSPER)
Iowa State University
2711 South Loop Drive, Suite 4700
Ames, IA 50010-8664
Phone: 515-294-8103 / Fax: 515-294-0467
https://propser.intrans.iastate.edu

TABLE OF CONTENTS

LIST OF FIGURES

LIST OF TABLES

ACKNOWLEDGMENTS

The authors gratefully acknowledge the Iowa Department of Transportation (Iowa DOT) for sponsoring this research and the Federal Highway Administration (FHWA) for the state planning and research (SPR) funds used for this project.

The project technical advisory committee members, Ed Bartels, Brandon Billings, Lee Bjerke, Curtis Carter, Khyle Clute, Chris Cromwell, Alex Davis, Michelle Fields, Vanessa Goetz, Brian Keierleber (former Buchanan County Engineer), Todd Kinney, Ronald Knoche, Tim McClung, Matthew Miller, Wes Musgrove, Tammy Nicholson, Scott Nixon, Greg Parker, Jesse Peterson, Melissa Serio, Derek Snead, Wade Weiss, Cedric Wilkinson, Bob Younie, and Andrew Zimmerman, are gratefully acknowledged for their guidance, support, and direction throughout the study.

The authors acknowledge with deep appreciation the Iowa DOT's unwavering support, and this appreciation is extended to all the enthusiastic and hardworking Iowa DOT engineers and technicians who carefully carried out all field data collection. The authors would also like to express their sincere gratitude to the members of the Michigan Tech Research Institute (MTRI) research team that participated in this project and other research team members from the Program for Sustainable Pavement Engineering and Research (PROSPER) at the Institute for Transportation (InTrans) at Iowa State University (ISU) for their assistance.

EXECUTIVE SUMMARY

The increasing use of small uncrewed aircraft systems (sUAS), also known as drones, in transportation infrastructure monitoring has validated the critical importance of this technology in modern engineering practice. sUAS technology offers significant benefits, including cost efficiency, enhanced safety, and improved productivity. While these advantages align with the goals of the Iowa Department of Transportation (Iowa DOT), the integration of sUAS into routine engineering practices carried out by the Iowa DOT is yet to be fully explored.

During a Technical Advisory Committee (TAC) meeting held on April 8, 2025, the TAC expressed its interest in exploring the benefits of sUAS technology for monitoring gravel roads. Based on this interest, the research team conducted this second pilot project, whose primary aim was to evaluate the effectiveness of sUAS in assessing the overall conditions of gravel roads and for the ability of sUAS-based distress assessments to serve as a major part of Iowa's local community support.

Two sUAS, a FreeFly Astro equipped with a Sony ILX-LR1 61 MP red/green/blue (RGB, or natural color) camera and a DJI Mavic 2 Enterprise Advanced (M2EA) equipped with a built-in 48 MP quad-bayer camera, were utilized for data collection. We collected data both manually and using the sUAS from four major gravel road sites in Iowa: (1) 130th Street, Buchanan County, (2) 150th Street, Buchanan County, (3) Frost Avenue, Buchanan County, and (4) Flemming Avenue, Story County. While the sUAS were flown at 40 ft (12.2 m) at nadir for most of the distress assessments, the gravel road terrain dictated the altitudes and camera angles adopted for dust-focused sUAS data collection.

In this study, along with collecting sUAS data and processing images into digital elevation models (DEMs), hillshade images, and orthomosaic photos, we developed proof-of-concept pattern recognition algorithms integratable with ArcGIS Pro software for extracting gravel road distress features from the processed sUAS data. Overall, we collected datasets for rutting, corrugation, dust, crown, and potholes in a way that enabled comparisons between algorithmic and manual measurements. The prototype tools and algorithms developed in this study were used to detect and rate distress using elevation model data and color orthomosaics. The distresses of interest were rutting, corrugation, potholes, loose aggregate, and improper crown. In the limited test cases conducted for this pilot project, the proof-of-concept tools showed acceptable accuracy but room for improvement. The findings from the limited deployment of these tools are provided below:

- The developed proof-of-concept toolboxes for distress quantification showed promising results in detecting and quantifying distress severities from processed sUAS data, such as DEMs and orthophotos.
- The rutting tool measured slightly lower rutting values than those obtained through manual measurement but classified the observed rutting in the same severity levels. However, the detection and rating of low-severity rutting remains a challenge.

- The correlation between manual measurements of corrugation and automatic measurements from very high-resolution elevation data showed an R^2 value of 0.74. We anticipate a higher correlation in a more ideal scenario, free of moving traffic during data collection.
- Dust severities were categorized as No Dust, Low Dust, and High Dust, and the category detection algorithm was trained using a deep learning model (ResNet152), which yielded an F1 score of 0.95 on test dataset predictions.
- Foot-on-ground (FOG) measurements of pothole depth and width closely matched the measurements automatically extracted by the proof-of-concept toolbox, with R^2 values of 0.98 for depth and 0.91 for width.
- The loose aggregate prototype toolbox needs additional field measurements to validate and further refine the detection algorithm.
- We proposed a severity matrix for improper cross-section, and the profiles generated by the toolbox closely aligned with the manually measured points.
- A DEM resolution of 1.5 mm or better is recommended for better precision of distress quantification.
- Overall, the need for rapid maintenance interventions makes it challenging to develop a sufficiently large database for validating the proof-of-concept algorithm in this study.

This study showed that visual identification of some gravel road distresses, including dust, potholes, rutting, corrugation, improper cross-section, and loose aggregate, is possible when color images and elevation data are analyzed using the developed proof-of-concept tools, which demonstrated promising performance for distress detection and quantification.

INTRODUCTION

Background and Problem Statement

The extensive use of small uncrewed aircraft systems (sUAS), commonly known as drones, in the transportation industry for remote sensing and infrastructure monitoring has validated the critical importance of this technology in modern engineering practice (Watts et al. 2012). This technology has been adopted by both government agencies and private entities responsible for highways, bridges, transportation infrastructure, and airports (Banić et al. 2019, Fischer et al. 2020, Flammini et al. 2016, Mitra et al. 2025, Nooralishahi et al. 2021, Oguntoye et al. 2025, Pietersen et al. 2022, Sourav et al. 2024, Tan and Li 2019).

For example, a wide variety of studies have been conducted on airfield pavement damage detection and rating and on the long-term use of sUAS to complement traditional infrastructure inspection processes (Oguntoye et al. 2023, 2025; Pietersen et al. 2022; Sourav et al. 2022, 2023a, 2023b, 2023c, 2024; Vidyadharan et al. 2017). These studies have also provided guidelines for adoption and have explored future potential applications (Sourav et al. 2024). In addition, multiple studies in the United States and elsewhere have reported on the increasing use of sUAS for the inspection of highway technology, including railway infrastructure, where it enables efficient monitoring of tracks, bridges, and overhead structures. Studies have also demonstrated its effectiveness in detecting track defects, inspecting tunnels, and assessing vegetation encroachment, all of which reduce the need for manual inspections and minimize service disruptions (Aela et al. 2024, Banić et al. 2019, Flammini et al. 2016).

Iowa is predominantly an agriculture-based state with approximately 70,000 mi of gravel roads that account for about 60% of all roads in the state (ICEA n.d.). Such roads provide adequate and cost-efficient infrastructure for transportation services in rural areas with low traffic volumes. For example, according to Breitenbach (2017), the cost of resurfacing a paved road in Allamakee County, Iowa, was estimated at $100,000/mi in 2011, while the cost of converting an already paved road to a new gravel road was only $5,000/mi. Although gravel roads require significantly lower construction costs compared to paved roads, they deteriorate at a faster rate due to heavy agricultural traffic loads and freeze-thaw and wet-dry cycles (Alzubaidi and Magnusson 2002) and therefore require frequent maintenance activities to keep them in working condition (Alzubaidi and Magnusson 2002). According to a recent estimate, Iowa's county road departments spend more than $145 million annually on maintenance costs, including more than $35 million for snow removal and more than $110 million for resurfacing/regrading (InTrans 2021). The wide range in the quality, supply, and price of granular material available in different regions of the state can result in significant differences in the level of service.

Routine distress assessment of granular roads is therefore crucial, because road distress can reflect inadequate design criteria, insufficient crown, inferior drainage, and a lack of strength in the pavement layers due to poor gravel quality and insufficient layer thickness (Huntington and Ksaibati 2015). Inspecting transportation infrastructure is a routine task performed by state department of transportation (DOT) engineers to assess structural health and plan maintenance schedules, and these inspections have traditionally been conducted manually, requiring

significant resources in terms of personnel, cost, and time as well as measures to ensure safety and minimize traffic disruption (Sattar et al. 2018). Given the challenges of balancing these priorities, sUAS technology presents a promising solution, with previous work by Michigan Technological University team members having shown initial promise (Brooks et al. 2016, Dobson et al. 2014).

While the capabilities of sUAS align with the goals of the Iowa Department of Transportation (Iowa DOT) regarding transportation infrastructure assessment, questions remain about how to integrate sUAS technology into gravel road distress-monitoring practices. Low-volume gravel roads are often inspected visually by human inspectors. Such traditional methods offer close-up visual inspection capabilities, but the challenges of achieving accurate information significantly scale up as the number of road miles increases and as distresses becomes more numerous and spatially diverse. The application of sUAS to this task helps collect field data as-is and thereby offers numerous opportunities for remotely assessing the condition of a gravel road at any point and at any time. The use of sUAS also helps prevent injuries and illnesses caused by exposure to dust, hazardous animals (e.g., snakes, falcons, raccoons), and toxic plants (e.g., poison ivy, poison oak, thorns) (Hubbard et al. 2017). Based on past and current trends, sUAS technology offers numerous benefits, including cost optimization, enhanced safety, and improved productivity (McGuire et al. 2016).

Several published manuals guide the rating of gravel road conditions. Popular among them are the U.S. Army Corps of Engineers (USACE) *Unsurfaced Road Maintenance Management* manual (Eaton and Beaucham 1992) and the *Pavement Surface Evaluation and Rating (PASER)* manual from the University of Wisconsin–Madison Transportation Information Center. While the latter provides a quick assessment tool, the former allows for in-depth measurement of each distress-critical feature to estimate overall condition. Therefore, in this task report we have leveraged the USACE technical manual, which also identifies seven key gravel road distresses and prescribes guiding metrics for the categorization of severity levels into low, medium, or high.

We adhered to the following framework in our adoption of sUAS for monitoring gravel road distress:

1. Development of sUAS data collection strategies suitable for each distress.
2. Processing of sUAS image data into orthomosaics/orthophotos, digital elevation models (DEMs), and hillshade geospatial raster layers.
3. Testing of proof-of-concept toolboxes that extract distress features from the processed sUAS data using pattern recognition and computer vision models.
4. Integration of knowledge extraction tools in geographic information systems (GIS)-based software for faster testing and demonstration.
5. Development of a web application that enables distress detection toolboxes to be applied to any portion of the processed sUAS data for a gravel road.

Goals and Objectives

The overall objective of this pilot study was to evaluate the application/adoption of sUAS technology and its data in identifying and rating gravel road distress. To achieve the objective, the following goals were established:

- Conduct strategic and site-suited sUAS data collection and processing to generate high-quality sUAS data products.
- Develop a fast and easy-to-use proof-of-concept algorithm to identify and rate identified distress.
- Explore the use of a web application for the practical application of the distress toolboxes by Iowa county engineers.

STUDY AREA

We visited gravel roads in Iowa that were either recommended by county engineers or observed while driving around the Iowa State University area. For example, upon request for sites with typical gravel road distress that have not yet been graded or maintained, the Buchanan County Engineer, Brian Keierleber, recommended that the gravel roads on 130th Street (between Grant Avenue and Henley Avenue) and 150th Street (approaching Amish Boulevard) in Buchanan County be addressed. While the 150th Street gravel road had developed corrugation and a significant number of potholes, the 130th Street gravel road had developed frost boils and rutting. Comparing the two sites, we noticed that the 150th Street gravel road generated more activated dust when driven on at 25 mph, though the level was still minimal. We measured the crown (cross-section) on 150th Street, and since we needed additional data for dust categorization, we identified other gravel roads in Iowa, including (1) Flemming Avenue, Story County, and (2) Frost Avenue, Buchanan County, that generated more dust. Figure 1 and Figure 2 provide overviews of the locations and field photos of the gravel roads.

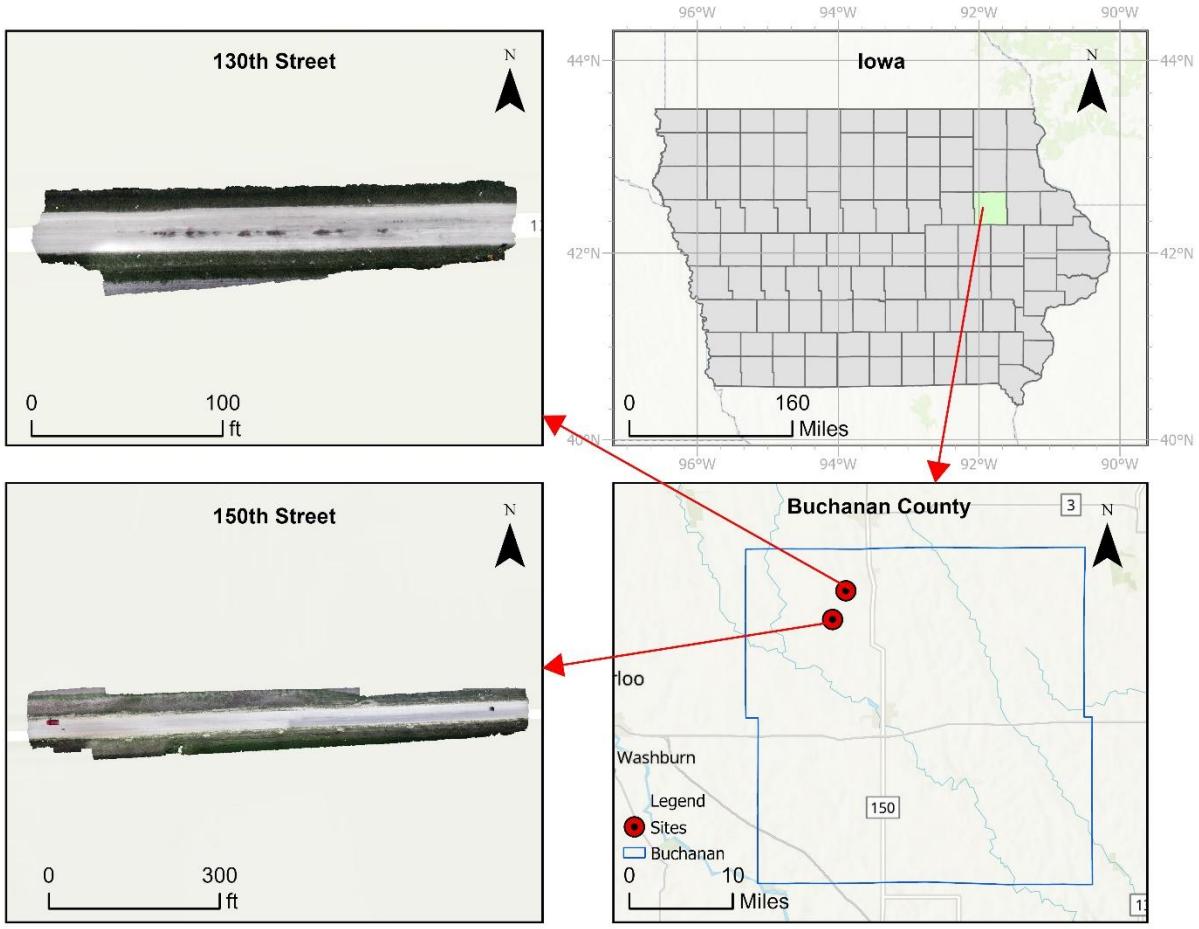

Figure 1. Overview of the 130th and 150th Street sites, including orthomosaics

Figure 2. Field photos captured during ongoing data collection at Iowa gravel road sites

DATA COLLECTION AND PROCESSING

On May 14, 2025, the Iowa State University (ISU) research team conducted sUAS-based remote sensing data collection along the two selected gravel road segments in Buchanan County, Iowa. The objective of this effort was to evaluate the feasibility of using small sUAS to visually assess gravel road surface condition, texture uniformity, rut depth indicators, and overall roadway shape. The collected imagery and ground control data were later processed in Agisoft Metashape to generate high-resolution orthomosaics and DEMs for further analysis. At each site, Propeller AeroPoint ground control points (GCPs) were positioned at intervals along the right-of-way to improve the geospatial accuracy of the processed dataset. The AeroPoint GCPs collected global navigation satellite system (GNSS) observations during flight operations that were later uploaded and processed to produce accurate coordinate solutions used during photogrammetric alignment.

sUAS Data Collection

All flights were performed using a FreeFly Astro equipped with a Sony ILX-LR1 camera with a 35 mm fixed focal length lens. The camera was operated in nadir capture mode to provide a consistent perspective for orthophoto generation. Three gravel road datasets were collected as part of this effort, and a summary of the altitudes flown and areas covered is provided in Table 1. Figure 3 shows the entire sUAS image collection pattern, along with ground control points, across the selected sample section of 150th Street in Buchanan County.

Table 1. sUAS data collection summaries with altitude flown and are covered

Location	Number of Images	Flight Altitude ft (m)	Coverage Area ha (m^2)
150th St	316	60 (18.3) AGL	~0.8214 (8,214)
150th St	366	40 (12.2 m) AGL	~0.8214 (8,214)
130th St	92	40 (12.2 m) AGL	~0.1139 (1,139)

AGL = above ground level

Figure 3. sUAS image points on 150th Street, Buchanan County, Iowa, with ground control points represented with flags

Data were collected under favorable wind conditions, which provided good flight stability and image clarity. Flight paths were flown at 80% forward and 70% side overlap to ensure high-quality orthophoto reconstruction.

Data Processing

All datasets were processed using Agisoft Metashape Professional (v2.2.1) on a workstation equipped with an Intel Xeon W-2265 processor, 128 GB RAM, and an NVIDIA Quadro RTX 5000 GPU. The processing workflow included the following standard photogrammetric steps:

- **Image Alignment**: Key point and tie point limits were set to 40,000 and 4,000, respectively. All images were successfully aligned for each dataset.
- **Dense Point Cloud Construction**: Depth maps were generated using high-quality and mild filtering, producing dense, high-resolution ground surface representations.
- **DEM Creation**: DEMs were generated directly from the dense clouds to characterize surface shape, drainage, rutting, and crown structure using elevation data.
- **Orthomosaic Generation**: Orthomosaics were created using the mosaic-blending mode, producing seamless, georeferenced 2D visual roadway datasets. Figure 4 shows the orthophoto generated for 150th Street, Buchanan County, Iowa.

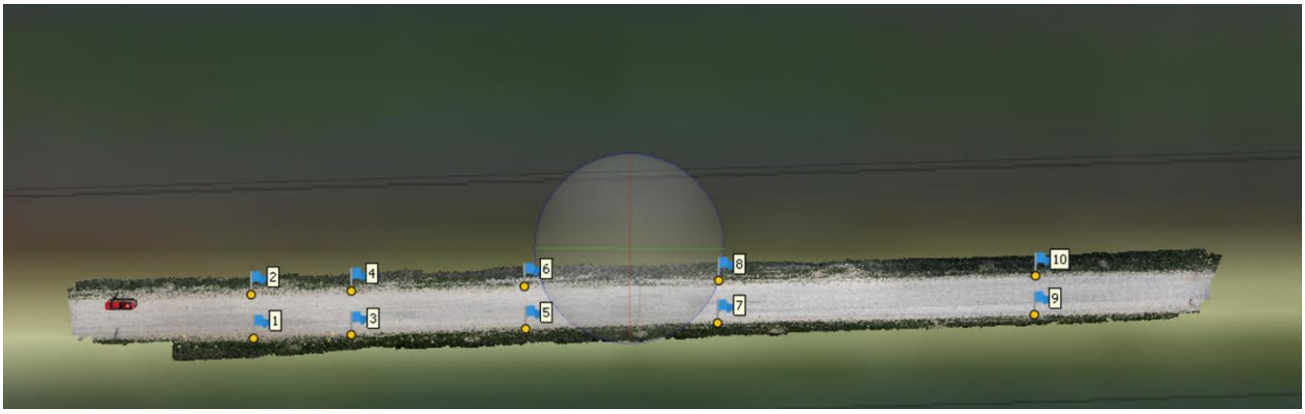

Figure 4. Processed orthophoto of 150th Street, Buchanan County, Iowa

A summary of key resulting resolutions from the generated metashape reports is provided in Table 2. The high spatial resolution achieved in these datasets ensured that fine surface texture and distress characteristics could be reliably detected during subsequent automatic roadway condition assessment.

Table 2. Resulting resolutions from the sUAS data processing

Location	Number of Images	Flight Altitude ft (m)	DEM Resolution in./pix (mm/pix)	Ortho Resolution in./pix (mm/pix)
150th St.	316	60 (18.3) AGL	0.148 (3.77)	0.074 (1.89)
150th St.	366	40 (12.2) AGL	0.091 (2.32)	0.046 (1.16)
130th St.	92	40 (12.2) AGL	0.102 (2.58)	0.051 (1.29)

AGL = above ground level

DATA ANALYSIS

We investigated the feasibility of automating the detection and quantification of several types of unsurfaced road distress from the processed sUAS data, which included DEM, hillshade, and orthophoto images. This chapter summarizes the adopted framework for each automatic distress detection task. We also compared the manually measured distress data with the automatic detection results. Since we envisioned using a direct and seamless automatic quantitative approximation of the Unsurfaced Road Condition Index (URCI) as established in the USACE *Unsurfaced Road Maintenance Management* technical manual, we focused on determining the finite severity and density values required to determine the deduct value for the final URCI approximation. This chapter is organized into sections to clearly discuss the automation processes.

Rutting

Automatic rutting detection on road infrastructure from sUAS images and the resulting processed data have been explored in past studies. For example, Biçici and Zeybek (2021) experimented with different sUAS flight altitudes and automatically extracted rutting information from the processed point-cloud data using their proposed elevation-based algorithm. In a related study, Zeybek and Biçici (2020) adopted a commercial software package, Global Mapper, to measure the length and depth of manually identified rutting distress on a surfaced pavement from a digital surface model. However, since little to no subsequent attention had been paid to automatic monitoring of gravel road rut distress, we developed a rut detection algorithm that requires users or pavement engineers to identify only the desired area extent or sample unit. We identified rutting distress on a gravel road on 130th Street in Buchanan County, Iowa, to validate our algorithm's performance.

Rutting distress appears as depressions found along the wheel paths parallel to the road center (Eaton and Beaucham 1992). We followed the USACE technical guidelines in assessing the severity and overall deduct values resulting from the observed rutting distress, estimating the severity class (low, medium, or high) based on the elevation obtained from the DEM, and further estimated the width and length of each identified rut to approximate its area. As specified in the USACE technical manual, a low-severity rut depth is typically less than 1 in. (2.5 cm), a medium-severity depth is between 1 to 3 in. (2.5 to 7.5 cm), and a high-severity depth is greater than 3 in. (7.5 cm), suggesting that, in terms of severity, the rutting should be measured in square feet. For example, a sample unit may have 75 ft^2 of high-severity rutting. Figure 5 illustrates the severity levels of ruts provided in the USACE technical manual. Since our algorithm bins detected rut patterns according to three severity classes, we bounded the low-severity rutting between 0.5 in. (1.27 cm) and 1 in. (2.5 cm), ensuring that unrutted regions are not classified as low rutting distress.

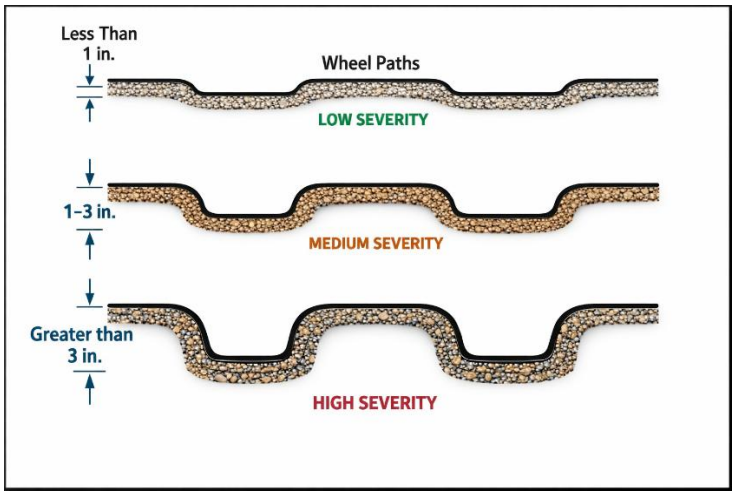

Eaton and Beaucham 1992

Figure 5. Rut severity illustration

Our proof-of-concept algorithm's accuracy directly relies on the resolution of the DEM data. Following the idealized rut pattern illustrated in Figure 5, we developed our rut detection toolbox to track ridges and intervening valleys, regardless of the roughness of the edges. To reduce false-positive detection, we assumed that the minimum height of the lower ridge sufficient for ponding and significant rutting should be 10% of the higher ridge level. The workflow of the adopted logic is presented in Figure 6.

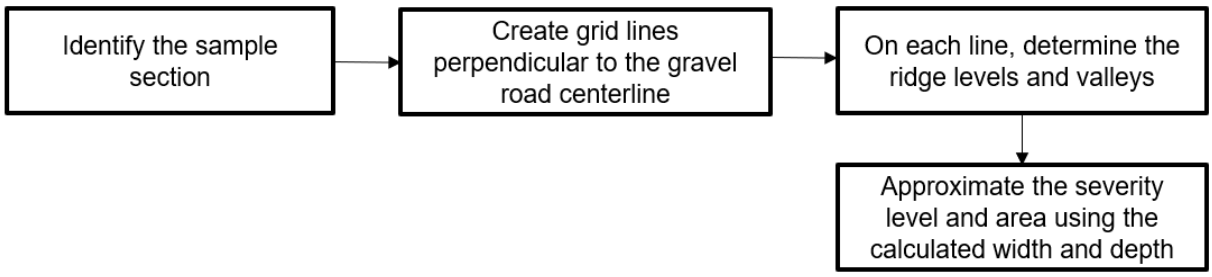

Figure 6. Workflow of proof-of-concept algorithm for detecting rutting severity

We created a customized toolbox in ArcGIS Pro by integrating the rut feature detection script. Figure 7 shows a screenshot of the toolbar that appears when the toolbox is launched, and Figure 8 provides further details about the required input parameters of the toolbox. Users of the toolbox are required to provide a polygon of the region of interest/sample unit, a DEM raster file of the gravel road, the sampling frequency per every 100 pixels in the DEM raster file, and the rutting width, which typically assumes constant and continuous rut features, as shown in Figure 8. Another feature we added is the ability to generate uncertainty and probabilistic awareness through automatic exploration of neighboring sampling frequencies. For example, if a user checks the box for neighboring sampling frequencies, the provided input neighbor range is applied to the original sampling frequency to determine the low and high bounds of frequencies with an interval of 1. As shown in Figure 7, the frequencies explored would be 1, 2, 3, 4, and 5 if

this box were checked. The tool presents the plots, results, and summary table for each severity class in HTML format, allowing users to interactively view the approximated numerical values. While the original HTML-formatted results for single-frequency sampling produce elevation plots and overall point estimates of severity per class, the neighboring sampling frequency technique provides the mean and standard deviation of severity per class, supporting better decision-making.

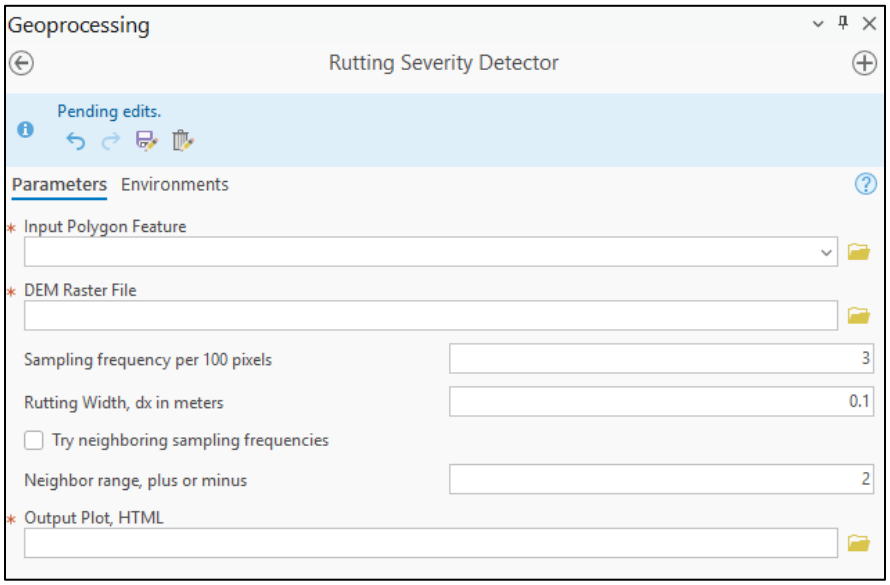

Figure 7. Screenshot of the customized proof-of-concept rutting severity detection toolbox

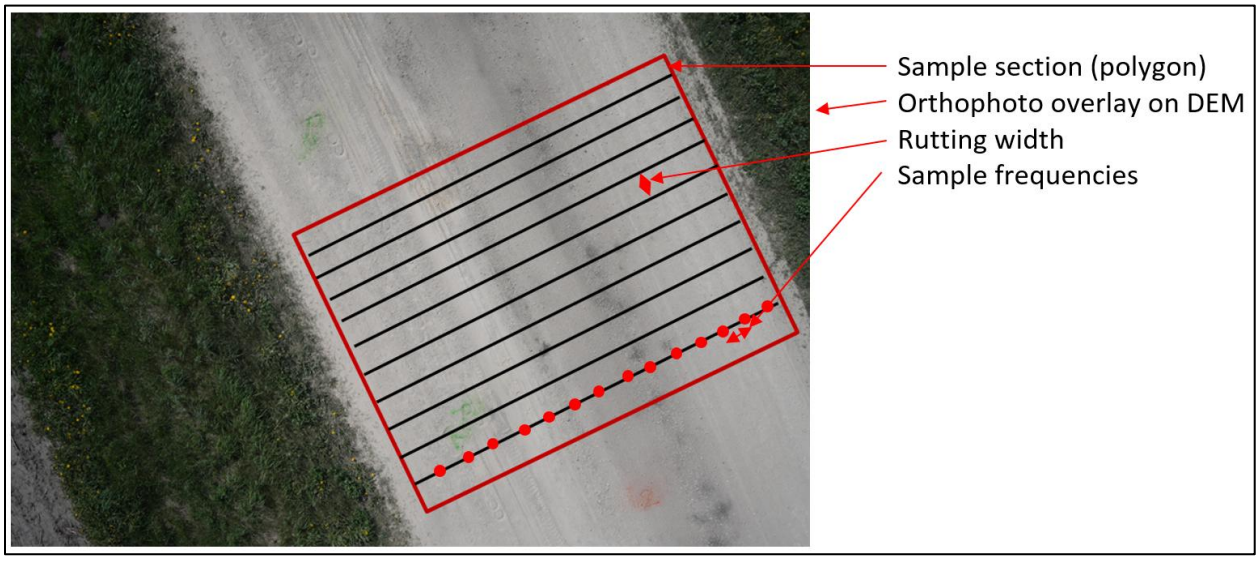

Figure 8. Detailed explanation of the proof-of-concept toolbox input parameters

We tested our proof-of-concept algorithm by comparing its predictions, shown in Figure 9, with manual measurements determined from the 130th Street DEM data by following ASTM E1703/E1703M-10, Standard Test Method for Measuring Rut-Depth of Pavement Surfaces

Using a Straightedge. The toolbox outputs an HTML file showing the cross-section profile of each supporting inner-working gridline, as well as a table summarizing the total severity, depth, and area of rutting when the neighboring sampling frequency box is unchecked. However, when the neighboring sampling frequency box is checked, the mean and standard deviation plots of the depth and total area per severity are provided. The output also includes the final total severity area per class to allow easier approximation of the deduct value needed to calculate URCI.

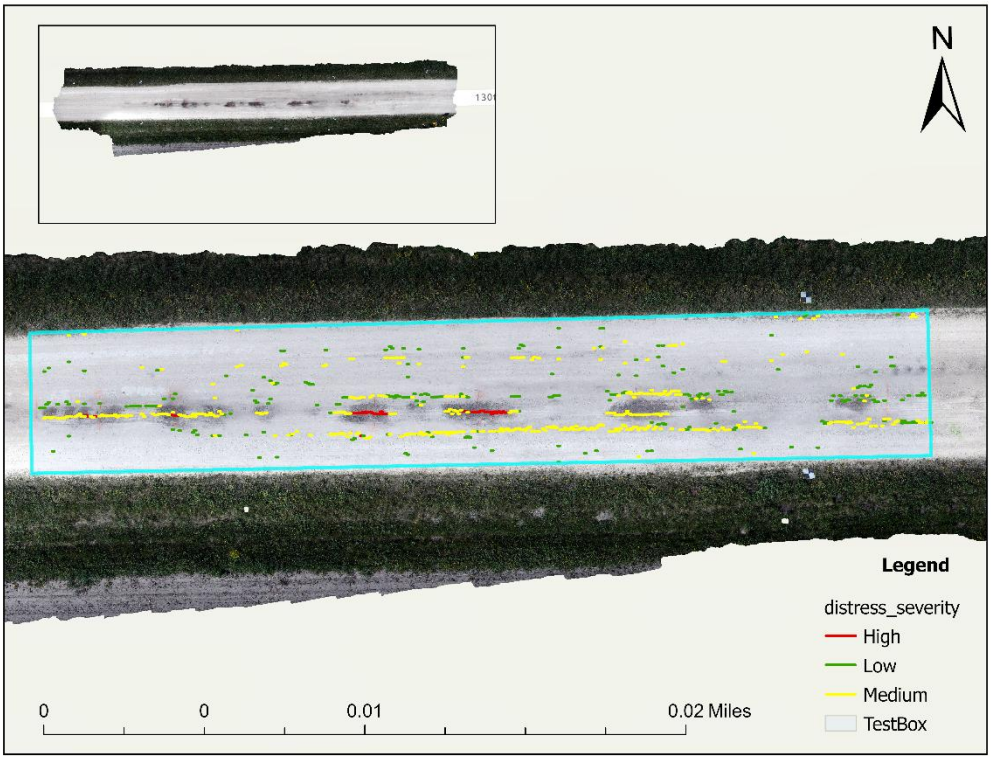

Figure 9. Screenshot of the area of interest for rutting detection bounded in a test box

Figure 10 and Figure 11 are screenshots from the HTML output files for both sampling cases. To ease rutting distress localization, our program adds feature layers to the map, showing regions of detected ruts. Finally, it is important to note that regions of frost boils are identified by the algorithm as high-severity rutting. While the user may constrain the expected wheel path region to better apportion rut regions, unsurfaced gravel roads are typically low volume and may lack a specific two-way traffic pattern. Therefore, we did not alter the algorithm, assuming that areas identified as high-severity rutting may instead indicate the frost boils.

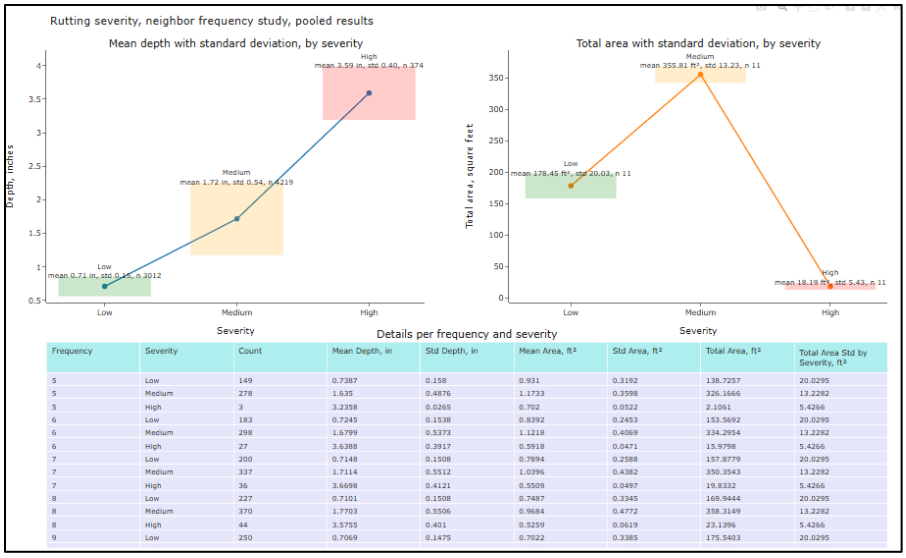

Frequency	Severity	Count	Mean Depth, in	Std Depth, in	Mean Area, ft²	Std Area, ft²	Total Area, ft²	Total Area Std by Severity, ft²
5	Low	149	0.7387	0.158	0.931	0.3192	138.7257	20.0295
5	Medium	278	1.635	0.4876	1.1733	0.3598	326.1666	13.2282
5	High	3	3.2358	0.0265	0.702	0.0522	2.1061	5.4266
6	Low	183	0.7245	0.1538	0.8392	0.2453	153.5692	20.0295
6	Medium	298	1.6799	0.5373	1.1218	0.4069	334.2954	13.2282
6	High	27	3.6388	0.3917	0.5918	0.0471	15.9798	5.4266
7	Low	200	0.7148	0.1508	0.7894	0.2588	157.8779	20.0295
7	Medium	337	1.7114	0.5512	1.0396	0.4382	350.3543	13.2282
7	High	36	3.6698	0.4121	0.5509	0.0497	19.8332	5.4266
8	Low	227	0.7101	0.1508	0.7487	0.3345	169.9444	20.0295
8	Medium	370	1.7703	0.5506	0.9684	0.4772	358.3149	13.2282
8	High	44	3.5755	0.401	0.5259	0.0619	23.1396	5.4266
9	Low	250	0.7069	0.1475	0.7022	0.3385	175.5403	20.0295

Figure 10. Screenshot from the HTML output with neighboring sampling frequency activated

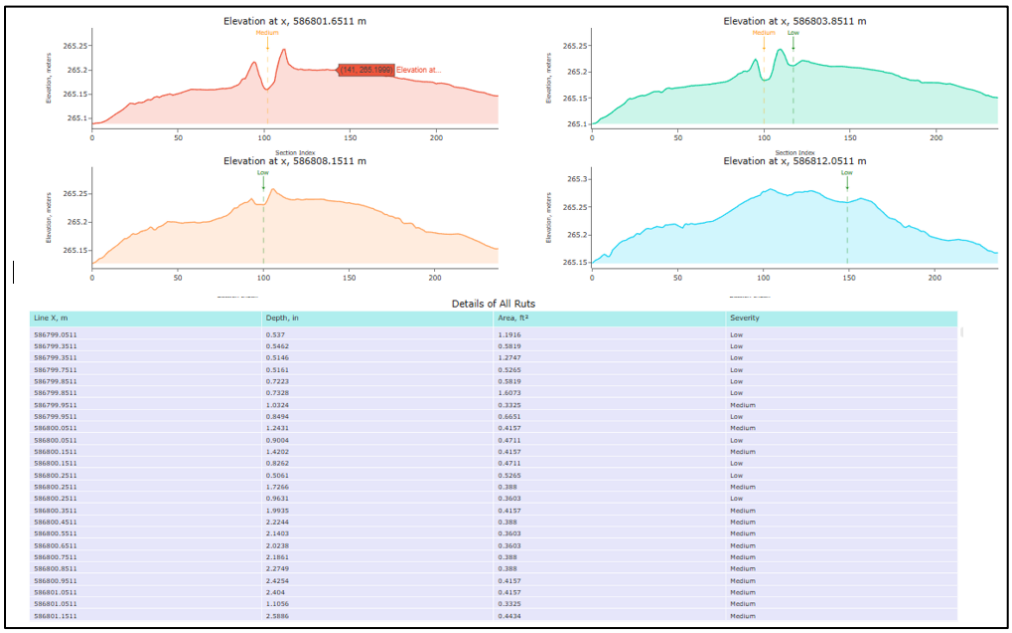

Line X, m	Depth, in	Area, ft²	Severity
586799.0511	0.537	1.1916	Low
586799.3511	0.5462	0.5819	Low
586799.3511	0.5146	1.2747	Low
586799.7511	0.5161	0.5265	Low
586799.8511	0.7223	0.5819	Low
586799.8511	0.7328	1.6073	Low
586799.9511	1.0324	0.3325	Medium
586799.9511	0.8494	0.6651	Low
586800.0511	1.2431	0.4157	Medium
586800.0511	0.9004	0.4711	Low
586800.1511	1.4202	0.4157	Medium
586800.1511	0.8262	0.4711	Low
586800.2511	0.5061	0.5265	Low
586800.2511	1.7266	0.388	Medium
586800.2511	0.9631	0.3603	Low
586800.3511	1.9935	0.4157	Medium
586800.4511	2.2244	0.388	Medium
586800.5511	2.1403	0.3603	Medium
586800.6511	2.0238	0.3603	Medium
586800.7511	2.1861	0.388	Medium
586800.8511	2.2749	0.388	Medium
586800.9511	2.4254	0.4157	Medium
586801.0511	2.404	0.4157	Medium
586801.0511	1.1056	0.3325	Medium
586801.1511	2.5886	0.4434	Medium

Figure 11. Screenshot from the HTML output without neighboring sampling frequency activated

Figure 12, Figure 13, Figure 14, and Figure 15 show the outputs for two of the three points (R2 and R3) sampled at the gravel road site, with the rutting line automatically overlaid on the map by our algorithm module. Due to the faintness of the color ramp used during manual rut measurement at the site, we were unable to locate the position of one of the points (R1) for comparison. Table 3 compares the manually measured and algorithmically measured depth and severity values for R2 and R3. The limited manually measured data points are insufficient to validate the proof-of-concept algorithm's accuracy and robustness. Therefore, future work

should consider visiting more gravel roads with varying severities of rutting distress to validate the developed algorithm.

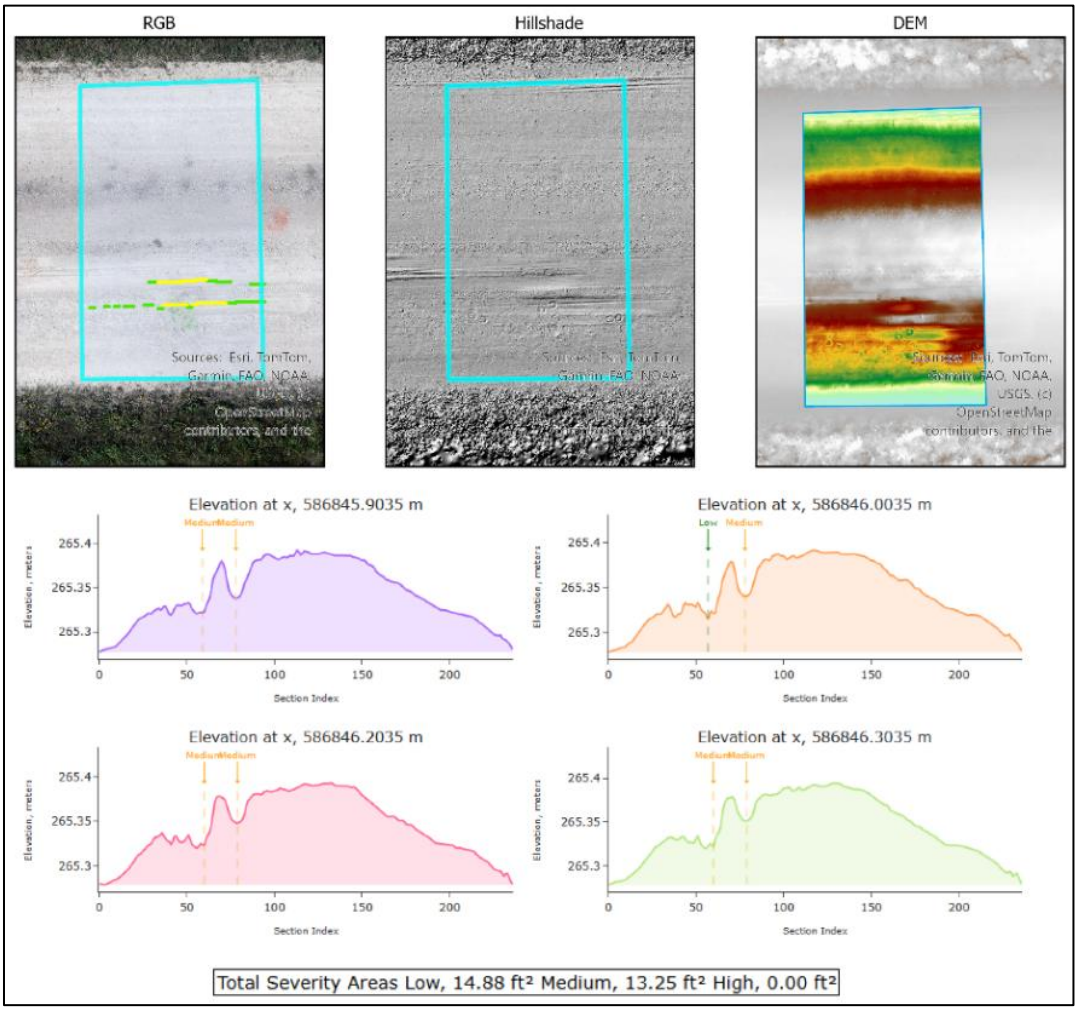

Figure 12. Algorithm output for manually sampled point R2 with randomly selected profile sections within the polygon (without neighborhood sampling frequency activated)

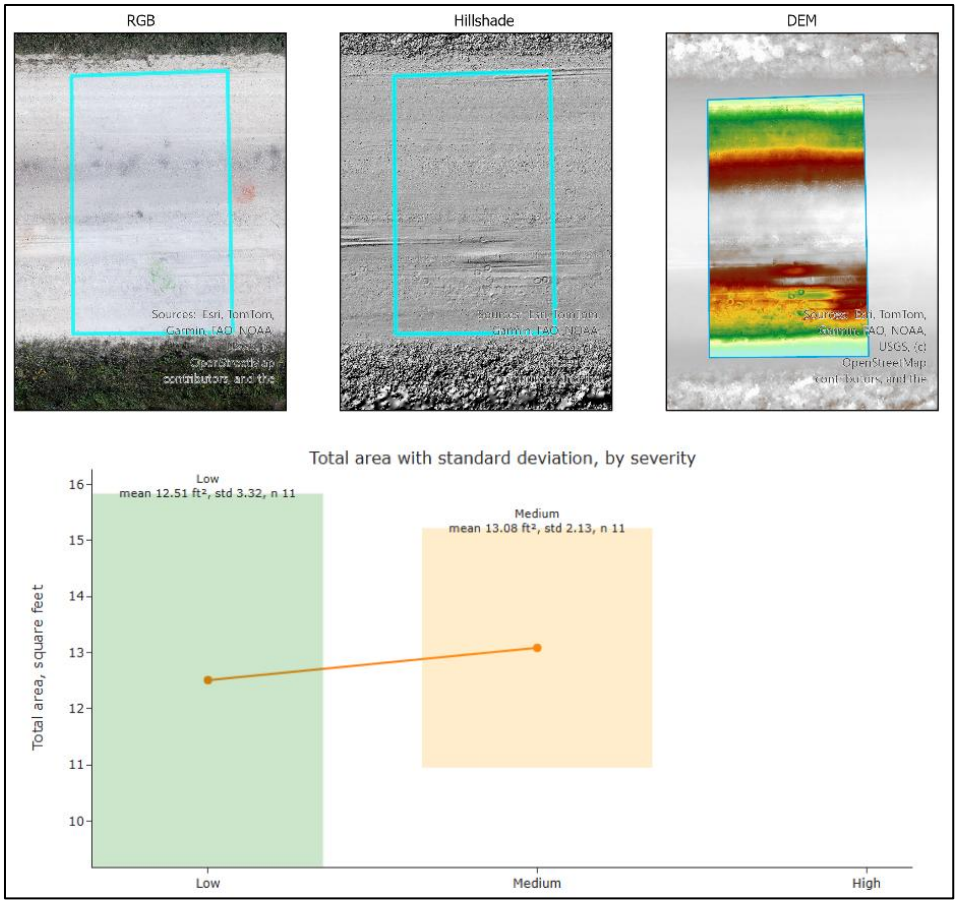

Figure 13. Algorithm output for manually sampled point R2 with the mean and standard deviation of each severity area (with neighborhood sampling frequency activated)

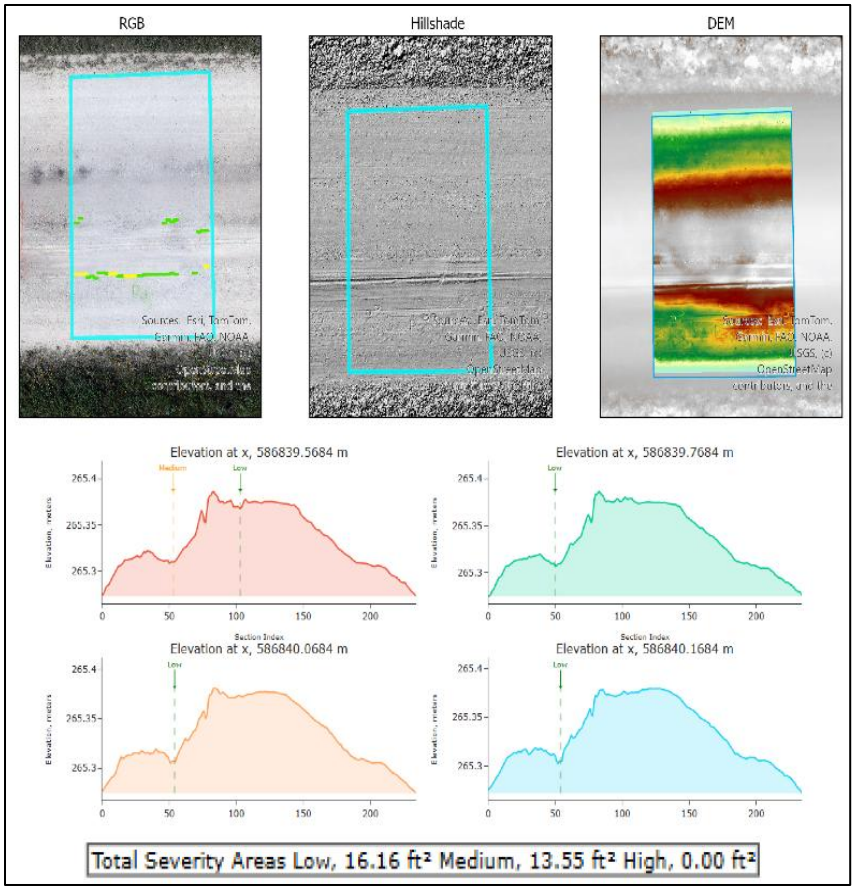

Figure 14. Algorithm output for manually sampled point R3 with randomly selected profile sections within the polygon (without neighborhood sampling frequency activated)

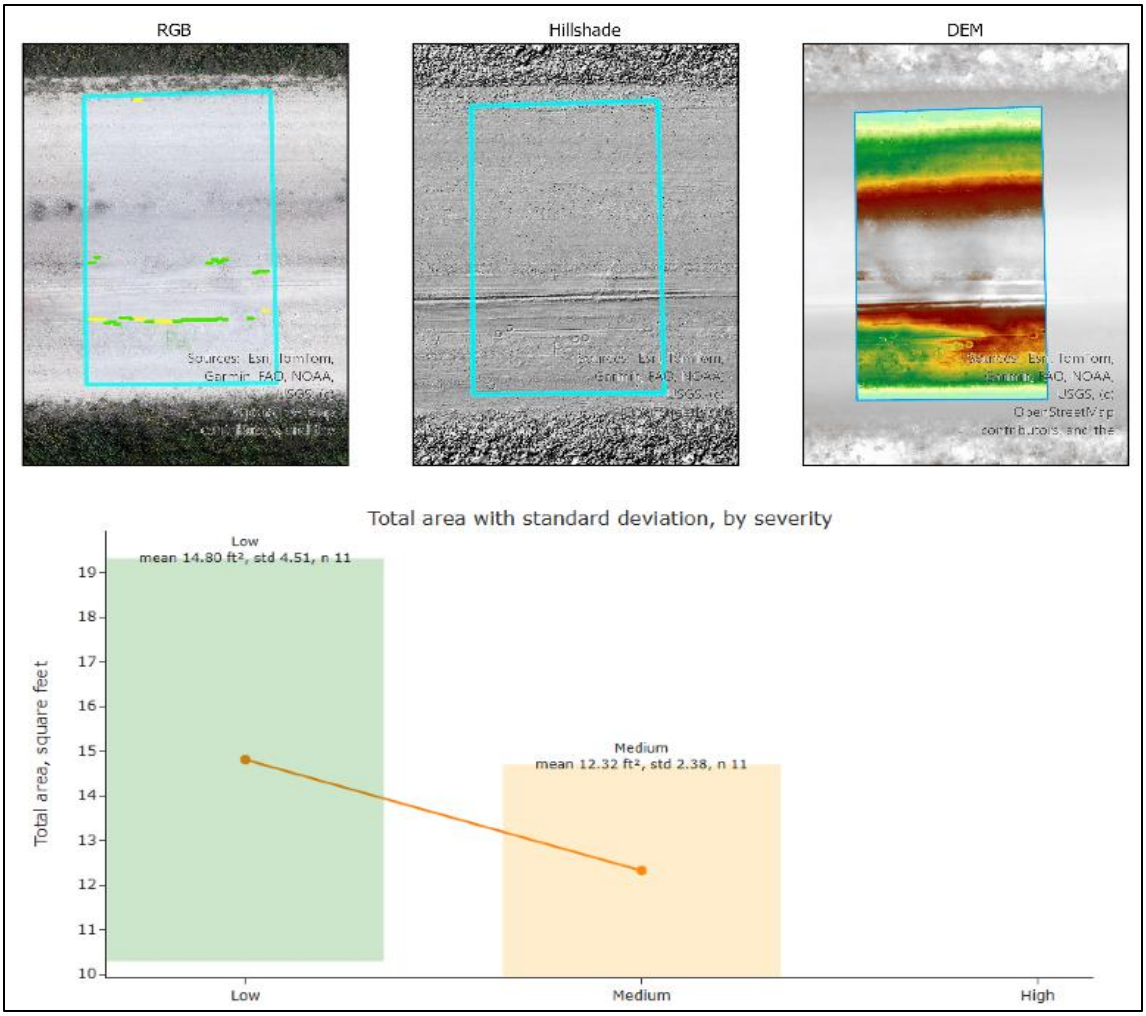

Figure 15. Algorithm output for manually sampled point R3 with the mean and standard deviation of each severity area (with neighborhood sampling frequency activated)

Table 3. Summary of manual and automatic rutting distress measurement

Sample Number	Manual (Point) Measurement (in.)	Algorithm (Point) Output (in.)	Difference (in.)	Severity Match
R1	1.0	-	-	-
R2	1.5	1.479	0.021	Medium
R3	1.0	0.7125	0.288	Low

While the R2 data point provides closer approximations of depth, similar severity classes are obtained for both R2 and R3, with the proof-of-concept toolbox showing promising capability for fast, remote measurement of the entire section's rutting to produce the final URCI approximation.

Corrugation/Washboarding

Similar to rutting detection, notable studies have been conducted on corrugation detection on both paved and unpaved roads. For example, several research studies have utilized image processing techniques and deep learning in identifying locations of corrugation distress on unpaved roads (Dobson et al. 2013, Lopes Amaral Loures and Azar 2023, Khilji et al. 2021, Zhang 2008). However, since image-based analysis is insufficient to accurately assess the extent of corrugation damage, which is necessary for categorizing the damage into severity levels and determining the area of a corrugated region, we quantified the extent of corrugation damage by utilizing the elevation data available in the DEMs produced when the collected sUAS images are processed in Agisoft Metashape (or other close-range photogrammetry software, such as Pix4D).

Corrugation is typically characterized by patterns of distress with spaced ridges and valleys at fairly regular intervals. It shares the same measuring method as rutting in terms of severity categorization and distress reporting in the USACE technical manual. The 150th Street gravel road in Buchanan County had the most significant corrugation among the visited gravel road sites. The severity categorization in the USACE manual, similar to that used for rutting, is illustrated in Figure 16. We formulated our proof-of-concept algorithm-based toolbox by reimagining corrugation distress as a rising and falling wave. As the wave progresses, different depths (troughs/valleys) are attained, revealing the severity class at each point. To facilitate rapid automated distress measurements within the sample unit, we developed a customized toolbox in ArcGIS Pro, whose algorithm's workflow is illustrated in Figure 17.

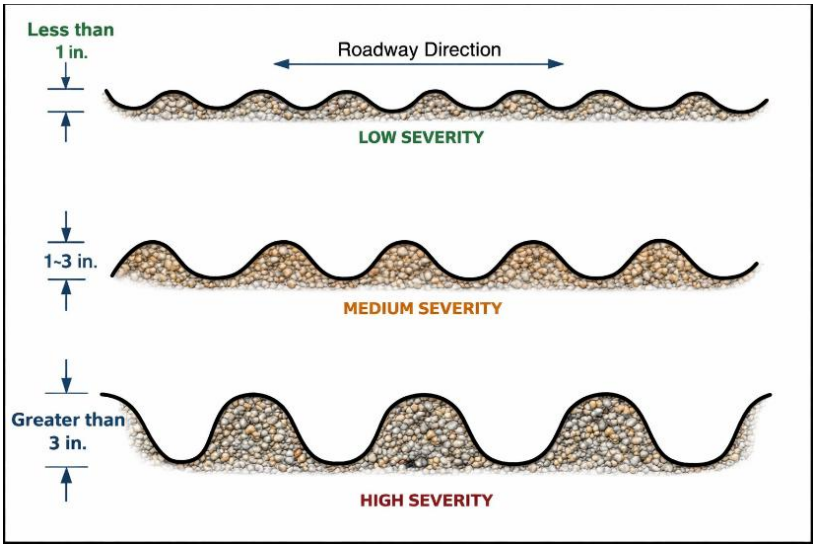

Eaton and Beaucham 1992

Figure 16. Severity levels of corrugation

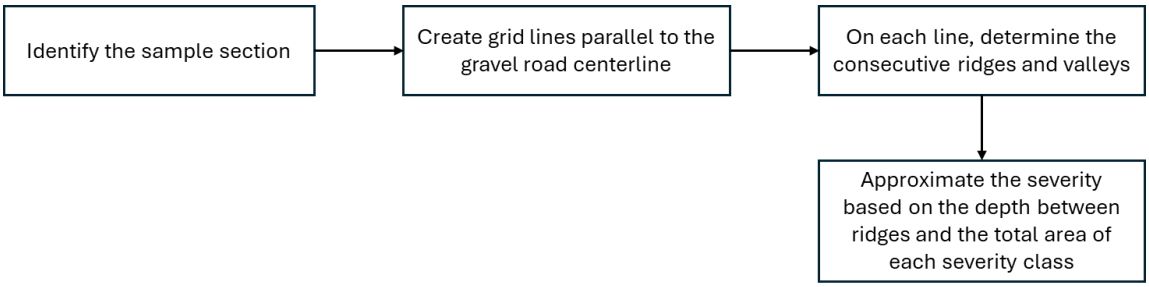

Figure 17. Workflow for the proof-of-concept corrugation detection toolbox

While the proof-of-concept workflow is similar to the rutting toolbox, in that it shares the same input features, we added Gaussian smoothing to simplify the aggregation of predefined corrugation patterns. The smoothening effect is controlled by the standard deviation input parameter for the Gaussian kernel (sigma), which determines the width of the kernel filter. The rule of thumb is that the wider the sigma, the stronger the smoothening effect on the input data. Screenshots of the customized toolbox and a polygon drawn over the orthophoto (with the DEM underneath) are shown in Figure 18 and Figure 19, respectively.

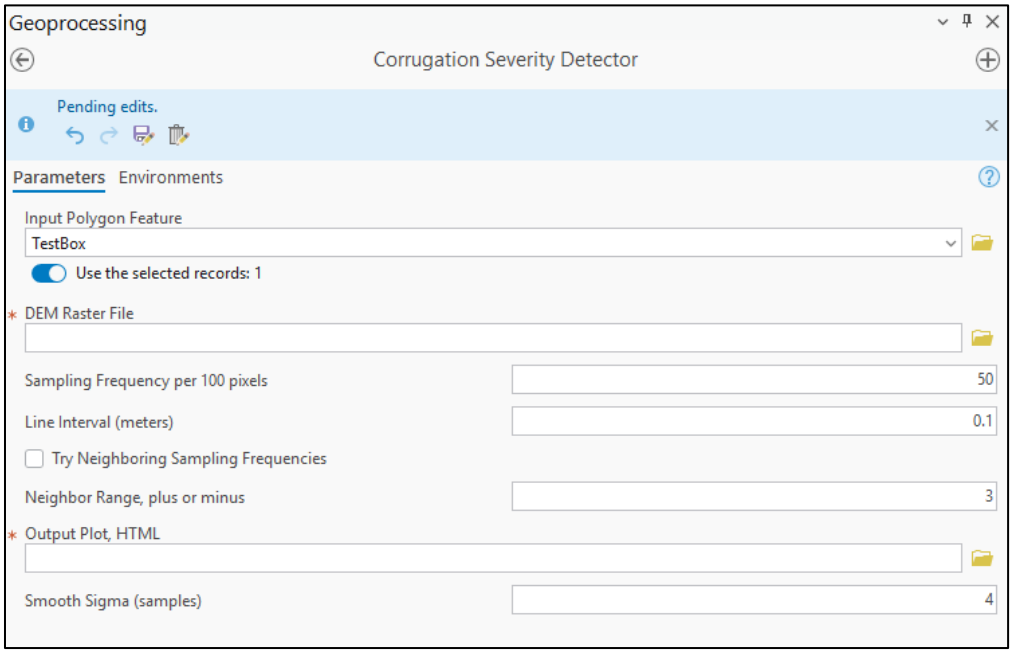

Figure 18. Screenshot of the proof-of-concept corrugation detection toolbox

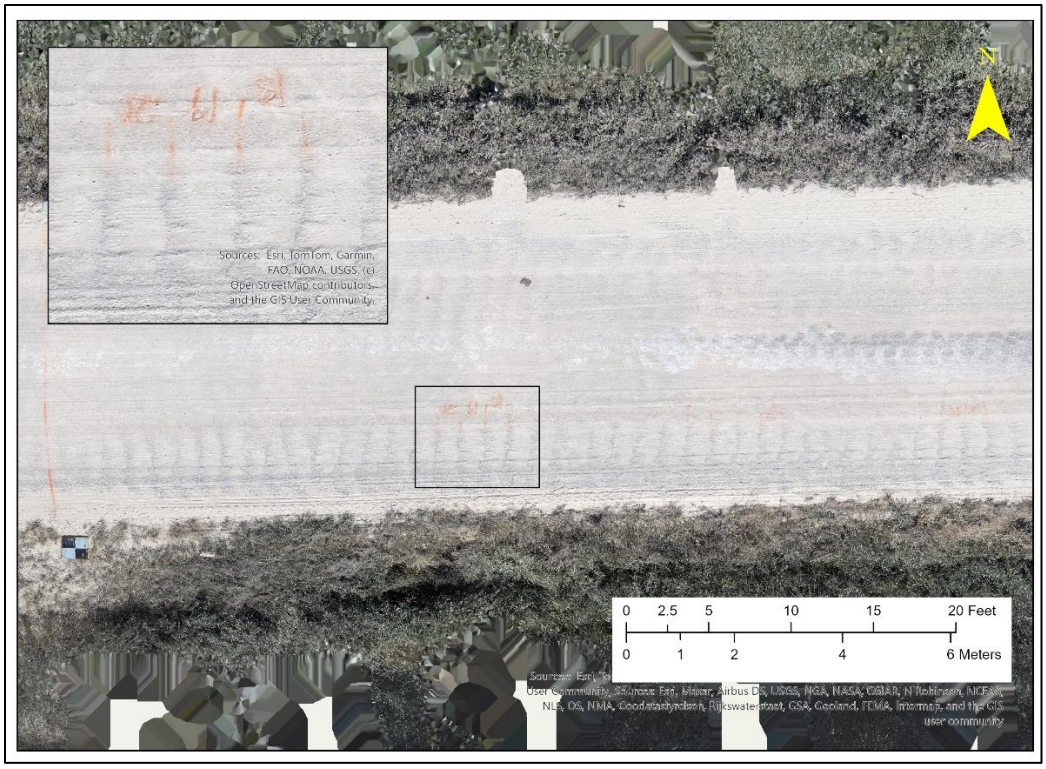

Figure 19. Screenshot of corrugation detection with an overlaid feature polygon

The proof-of-concept toolbox can generate different HTML outputs depending on whether the neighboring sampling frequency checkbox is activated, as in the rutting toolbox. If unchecked, the program uses a single sampling frequency and produces a plot like that shown in Figure 20, which includes the elevation plot, the smoothed elevation, and the severity plot across the horizontal guiding line. As observed in the small-region corrugation results, the results illustrated in Figure 21 show the probabilistic plot when neighboring sampling frequency is activated.

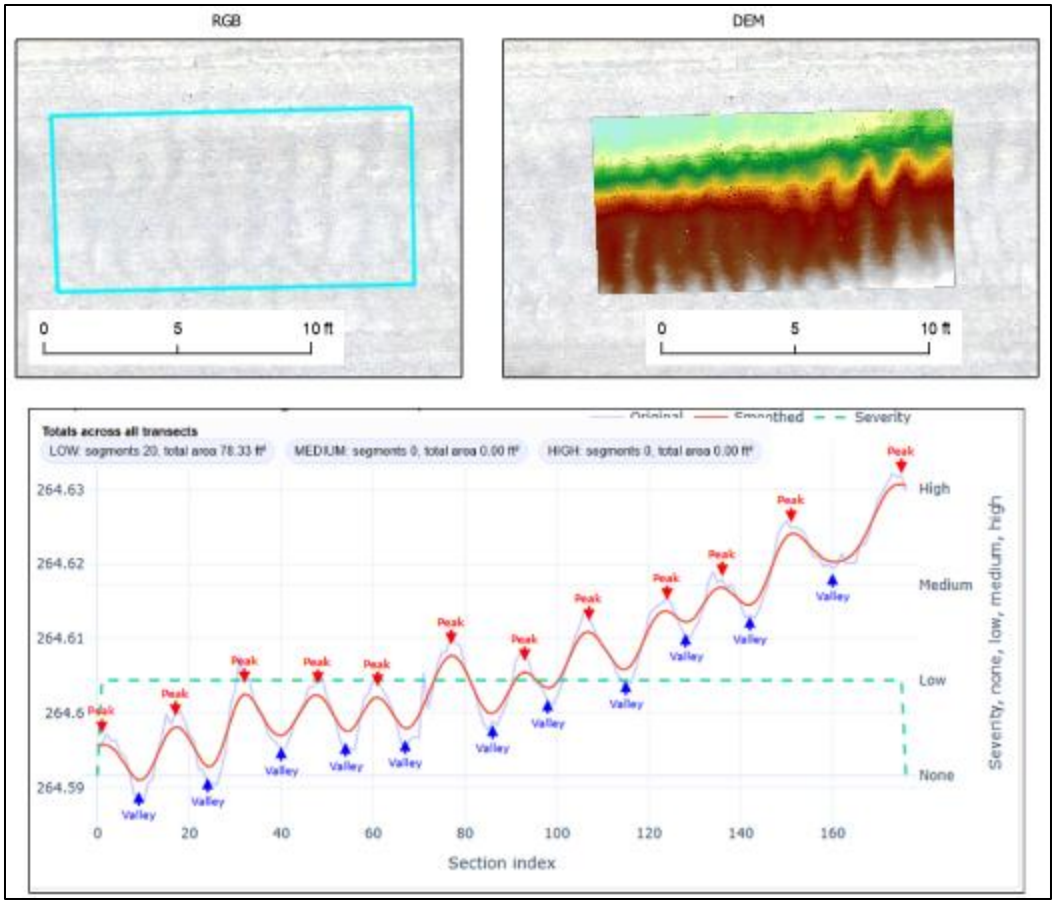

Figure 20. Screenshot of the HTML output file when neighboring sampling frequency is inactive

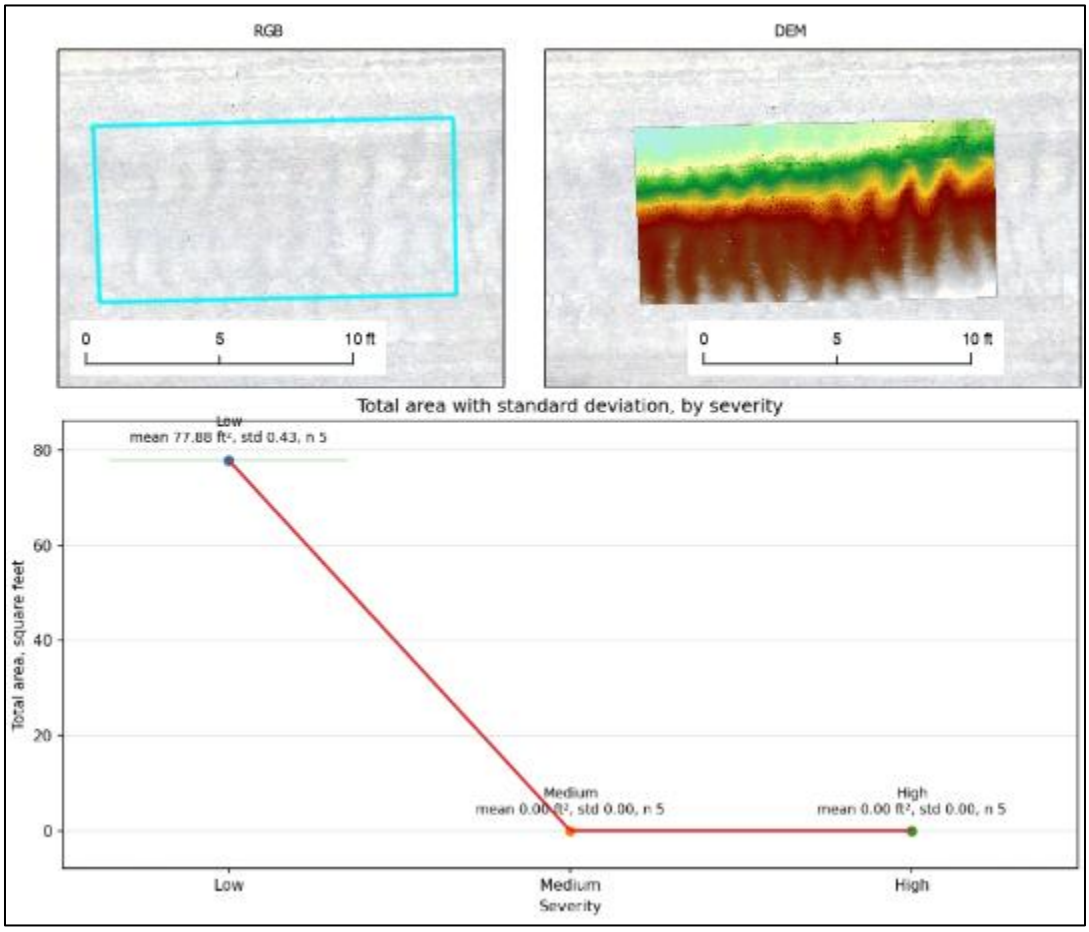

Figure 21. Screenshot of the HTML output file when neighboring sampling frequency is active

The corrugation results shown in Figure 20 and Figure 21 are in close agreement, with the latter providing standard deviation values for better decision-making.

We manually measured 20 points of corrugation depth between the ridges and compared the results with the automatically derived depths. However, manually measuring all 20 points in the field was not only time-consuming but also unsafe for human observers due to moving traffic and dust stirred up by the traffic. The adoption of sUAS for these tasks would ensure that data are collected quickly and safely. The developed proof-of-concept corrugation detection algorithm outputs both the severity category and the extent of the distress, a task that would typically require significant time and personnel resources if done manually. Table 4 and Figure 22 present a comparison of the manually and automatically measured data points. We achieved an R^2 of approximately 0.74 from the comparison. Because the drone flight occurred after all 20 corrugated points had been marked, we suspected that traffic during the intervening period most likely altered the corrugation's ridge-and-valley geometries, resulting in the observed differences between the manually measured and automatically measured depth values. Similar to rutting

distress analysis using sUAS, the accuracy of corrugation analysis relies heavily on high-resolution DEM data.

Table 4. Measured corrugation depths

Point Number	Manual Depth	Automatic Depth	Absolute Difference
1	0.6	0.5	0.1
2	0.6	0.5	0.1
3	0.8	0.7	0.1
4	1.0	0.9	0.1
5	0.9	0.7	0.2
6	0.9	0.8	0.1
7	1.0	0.9	0.1
8	1.1	0.9	0.2
9	1.1	0.9	0.2
10	1.0	1.1	0.1
11	0.8	0.7	0.1
12	1.1	1.0	0.1
13	0.8	0.8	0
14	1.0	0.8	0.2
15	0.8	0.7	0.1
16	0.9	0.8	0.1
17	0.8	0.7	0.1
18	1.0	0.8	0.2
19	1.0	0.8	0.2
20	1.0	0.8	0.2

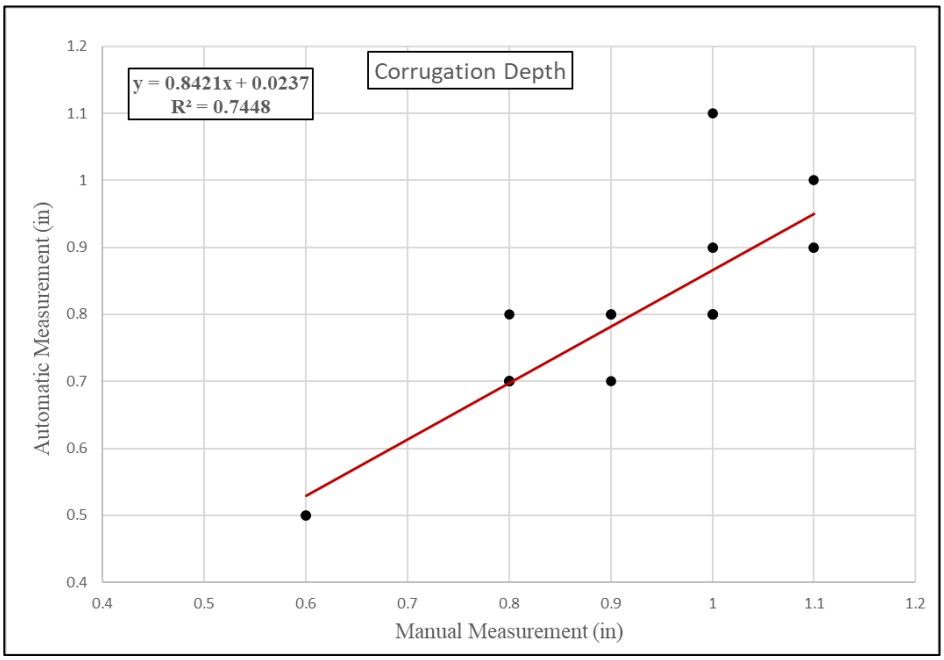

Figure 22. Manual versus automatic corrugation depth measurement

To ease visual detection of the corrugated points in the sUAS images, we expanded the detection tool by adding a feature that overlays corrugated points, as shown in Figure 23. The bounded region in Figure 23 is from the 150th Street data, with the majority of the corrugated points classified as low severity based on the algorithm's inferred depth.

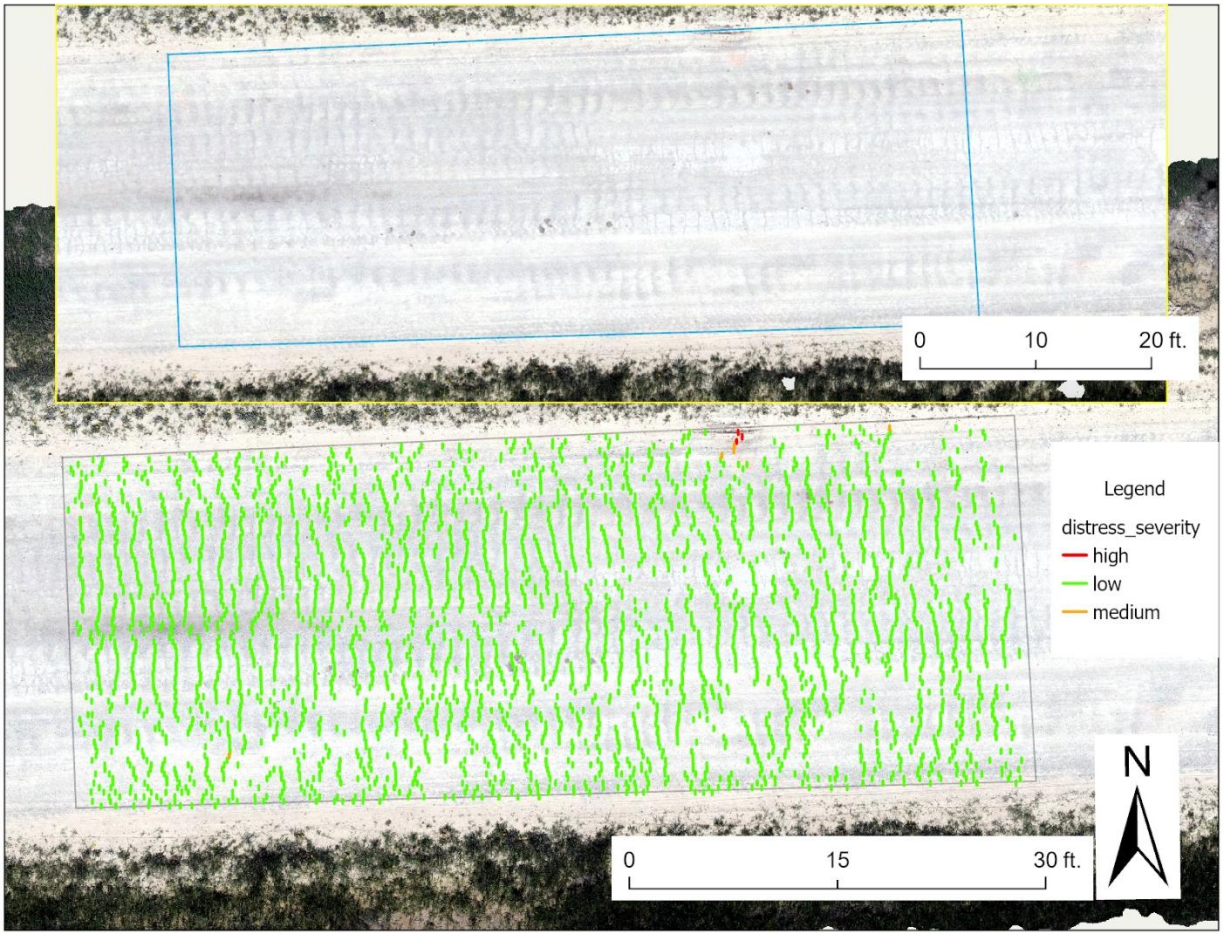

Figure 23. Sample output with overlaid corrugated points from the customized proof-of-concept toolbox

Dust

In addition to elevation-based pattern recognition, we developed a framework for classifying dust severity using color images and deep-learning models. As specified in the USACE technical manual, the severity level is determined by the visibility obstruction caused by the leading traffic at a speed of 25 mph. Based on this methodology, we adapted a method for dust data collection using sUAS. We identified a sample unit section during field data collection, then restricted our automatic detection framework to the sample unit by drawing a polygonal boundary using four key points, as shown in Figure 24. To capture the dust cloud trailing the leading traffic that generates the dust, we positioned the sUAS to hover in the sky with the camera capturing the leading traffic as it drove off.

Figure 24. Bounded sample unit for dust monitoring

We deployed YOLOv8, an off-the-shelf computer vision algorithm capable of different vision tasks, including object detection, to identify traffic in the sUAS images. We sought to detect the leading traffic as it encroached the predefined bounded region/sample unit. While YOLOv8 automatically detects moving vehicles and generates a tight-fitting bounding box around them, the goal in this case was to capture the trailing dust. We therefore adjusted and expanded the bounding boxes, then cropped out the regions of interest for further analysis. Figure 25 shows traffic detected within the bounded sample unit and the resulting cropped image after expansion. Given the possibility of failed detection, especially in edge cases where the dust cloud occludes the traffic in the image or the traffic appears small when far away from the camera, we developed the simple region-of-interest cropping mechanism illustrated in Figure 26. We were able to identify and crop the region of interest from every video frame using this technique.

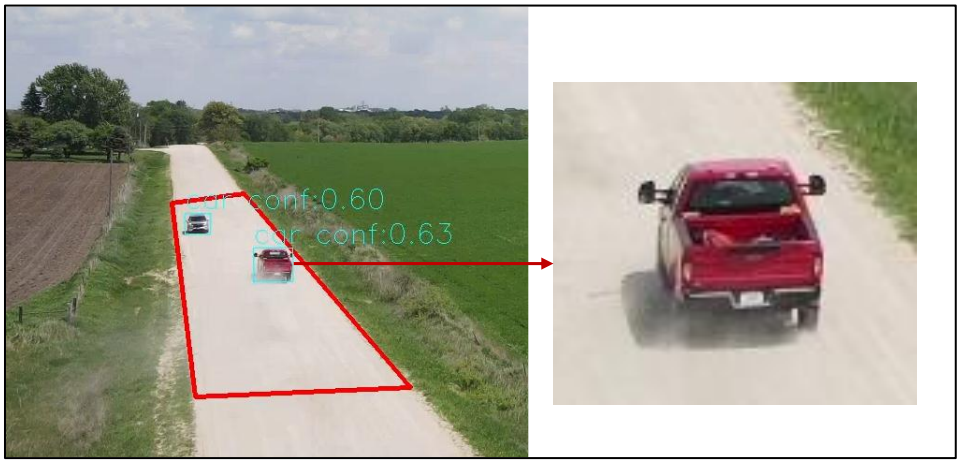

Figure 25. YOLOv8 detection within a bounded region (left) and a cropped, expanded region (right)

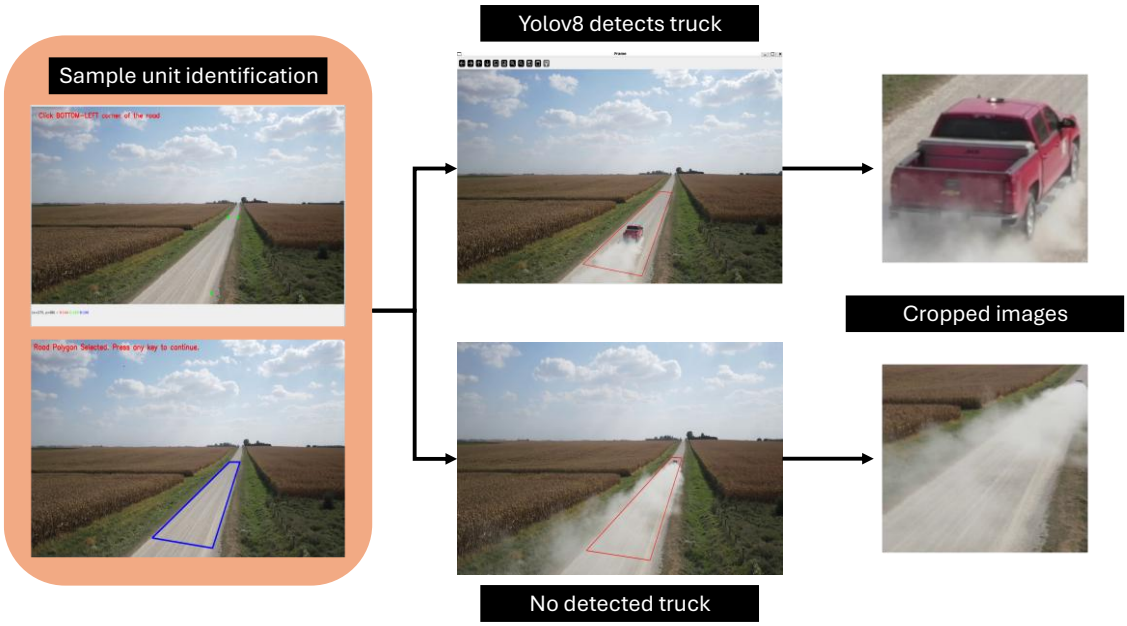

Figure 26. Cropping mechanism for sUAS video frames

At this stage, we resorted to training a deep-learning model to classify the severity level of the dust cloud visible in the video frame images into one of three major categories—No Dust, Low Dust, and High Dust—due to the challenges of distinguishing between the low and medium severity levels in the collected video images. We visited two additional gravel roads—Flemming Avenue, Story County, and Frost Avenue, Buchanan County—specifically for dust data collection. At the Flemming Avenue site, only a low-level dust cloud was activated when a truck was driven through at 25 mph. We decided to drive the truck through this site at 30, 35, 40, and 50 mph in controlled traffic, only within the sample unit, to gather enough data for classifying low-severity dust. The altitude at which the sUAS was flown at each site was dictated by the site terrain. In each case, we were specifically interested in a field of view that covered the sample unit of interest while also avoiding overhead electrical wires and other site-specific obstructions. Table 5 provides a summary of the data collection date, truck speeds, sUAS altitude, and number of recorded truck runs for each visited site.

Table 5. Selected sites for dust data collection on gravel roads via sUAS

Date	Gravel Road Site	Speed (mph)	sUAS Altitude (ft)	Truck Runs
October 02, 2025	Frost Avenue, Buchanan County	25, 50	20	2
June 24, 2025	Fleming Avenue, Story County	0 – 50	15	6
May 14, 2025	150th Street, Buchanan County	25	25	1

Since the images were collected at 30 frames per second, which sometimes made them appear static, especially when the trucks were driven at very low speeds, we sought to improve the robustness of our dataset by varying not only the speed but also the scene in each video. Figure 27 shows a detection and cropping process for dust data collection from Fleming Avenue, Story

County, that was similar to the process described above but with a different scene obtained by driving the truck through the site in the opposite direction. At Frost Avenue in Buchanan County, we encountered a gravel road with high dust levels even at 25 mph. We collected all high-dust-severity data from this site and also recorded dust activated by passing vehicles, providing a robust dataset for later training of the selected deep learning model.

Figure 27. YOLOv8 vehicle detection within a bounded region (Flemming Avenue, Story County)

We manually labeled all of the cropped images from the video frames in Label Studio, an open-source data annotation hub (Label Studio n.d.), and randomly selected images from the three categories to create the collages shown in Figure 28, Figure 29, and Figure 30.

Figure 28. No-dust images

Figure 29. Low-dust images

Figure 30. High-dust images

The training and testing data were carefully stratified to ensure robust validation of the trained model. Table 6 gives a summary of how the stratification was done for all of the recorded videos across the three sites visited for dust data collection. For this experiment, we adopted the ResNet152 model, a deep convolutional neural network that mitigates the vanishing gradient problem through the use of residual connections, enabling gradients to propagate effectively across its 152 layers (He et al. 2015). The pretrained backbone layers of the ResNet 152 model were frozen to retain the semantic feature representations learned from ImageNet, while the final fully connected layers were replaced with a custom classification head comprising a dense layer, a nonlinear activation function, and dropout regularization. This head produced the class logits, that were then passed through a cross-entropy loss function to estimate the posterior probability distribution over the three dust severity classes for each input image.

Table 6. Stratification of testing images (shaded cells) from the labeled and cropped images

Site	Video Files	Label	Image Count
Fleming Avenue, Story County	0 mph	No-Dust	949
	25 mph	No-Dust*	29*
		Low-Dust	179
	30 mph	No-Dust*	31*
		Low-Dust	206
	40 mph	No-Dust*	1*
		Low-Dust	102
	50 mph (south)	No-Dust*	1*
		Low-Dust	69
	50 mph (north)	No-Dust*	4*
		Low-Dust*	128*
150th Street, Buchanan County	25–35 mph	No-Dust	7
		Low-Dust	120
Frost Avenue, Buchanan County	25–50 mph (truck)	High-Dust*	593
	25–50 mph (trailer)		176*

* Test images

Upon completing the training of the adapted ResNet 152 model, we validated its performance using the stratified testing dataset. Table 7 provides a summary of the model's results when tested with the testing dataset using different metrics.

Table 7. Performance of the trained model across the test dataset

Label	Data Size	Per Class Result			Weighted Result			
		Precision	Recall	F1 Score	Accuracy	Precision	Recall	F1 Score
No Dust	66	0.9375	0.9000	0.9184	0.9467	0.9471	0.9467	0.9467
Low Dust	128	0.9038	0.9400	0.9216				
High Dust	176	1.0000	1.0000	1.0000				

While the performance shown in Table 7 indicates that the model can accurately distinguish between images with high dust levels compared to those with no or low dust, the consistently strong precision, recall, and F1 scores across all classes indicate that the classifier can reliably separate the three dust severity categories, with particularly robust and perfect performance for the high-dust class.

Potholes

Potholes are bowl-shaped depressions in the surface of a road, with severity levels categorized based on depth and diameter. A quick review of past studies in the literature reveals that most, if not all, automatic pothole detection tools, typically supported by image processing techniques and deep learning models, are designed for paved roads (Bosurgi et al. 2023, Bučko et al. 2022, Ma et al. 2022). While variation in pixel values, especially in pothole regions, makes the aforementioned techniques suitable when image/depth data are adopted, the USACE technical

manual for gravel road distress rating recommends measuring pothole distress by counting the number of potholes present and their severity. This implies that, beyond identifying the locations of these depressions, pothole distress assessment also involves extracting features that help categorize them by severity. We therefore leveraged a deep-learning detection module for automatic pothole detection that measured the diameter/width and depth of the bounded pothole regions in DEM data. The adopted framework for the automatic detection of pothole severity is illustrated in Figure 31.

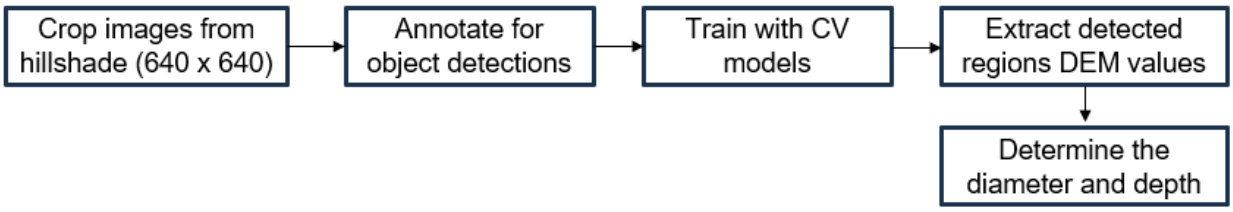

Figure 31. Workflow of the proof-of-concept pothole detection toolbox

A close comparison between hillshade and orthophoto images, as shown in Figure 32, shows that potholes are more pronounced in hillshade grayscale images because these images are generated from the DEM by simulating illumination from a chosen sun angle, thereby emphasizing local elevation changes. DEM gradients are converted to brightness values on a scale from 0 to 255, making small depressions and surface irregularities stand out more clearly than in orthophotos, which capture only surface color and texture.

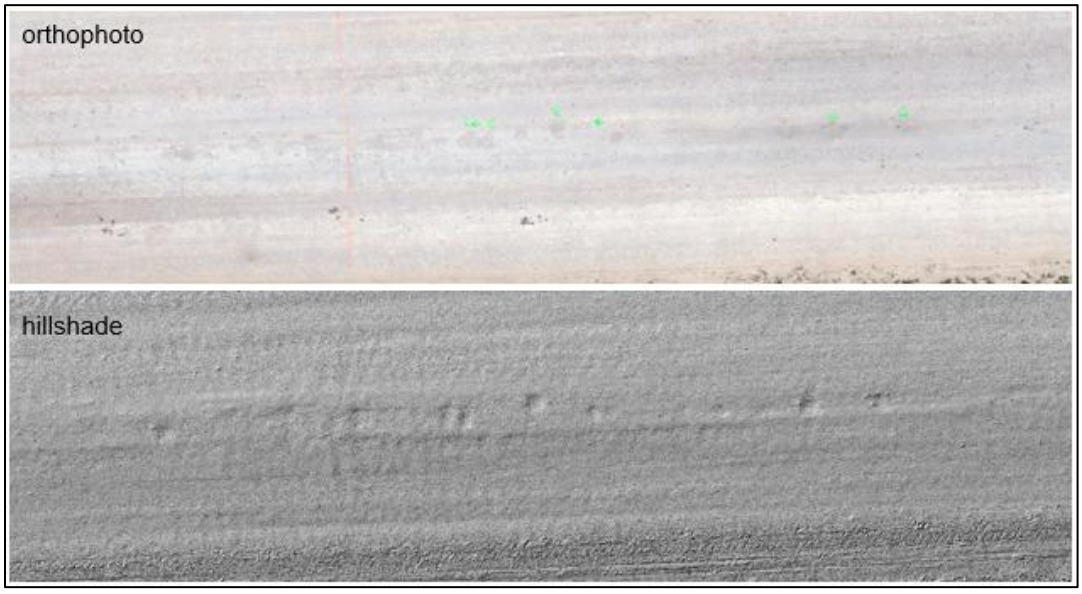

Figure 32. Orthophoto and hillshade images from 150th Street with pothole distress

We annotated about 150 cropped images by drawing polygons around the pothole regions for training. We trained a YOLOv5 model for automatic pothole detection, and the confusion matrix and sample predictions on the validation dataset are shown in Figure 33. When trained using only the 150th Street gravel road dataset, the model achieved a recall of 90% and an F1 score of

72.7%. The model's performance is expected to improve with the inclusion of additional high-quality processed sUAS data from gravel road sites containing a greater number of pothole distresses of varying severity levels, which would help reduce false positives and enhance overall detection accuracy.

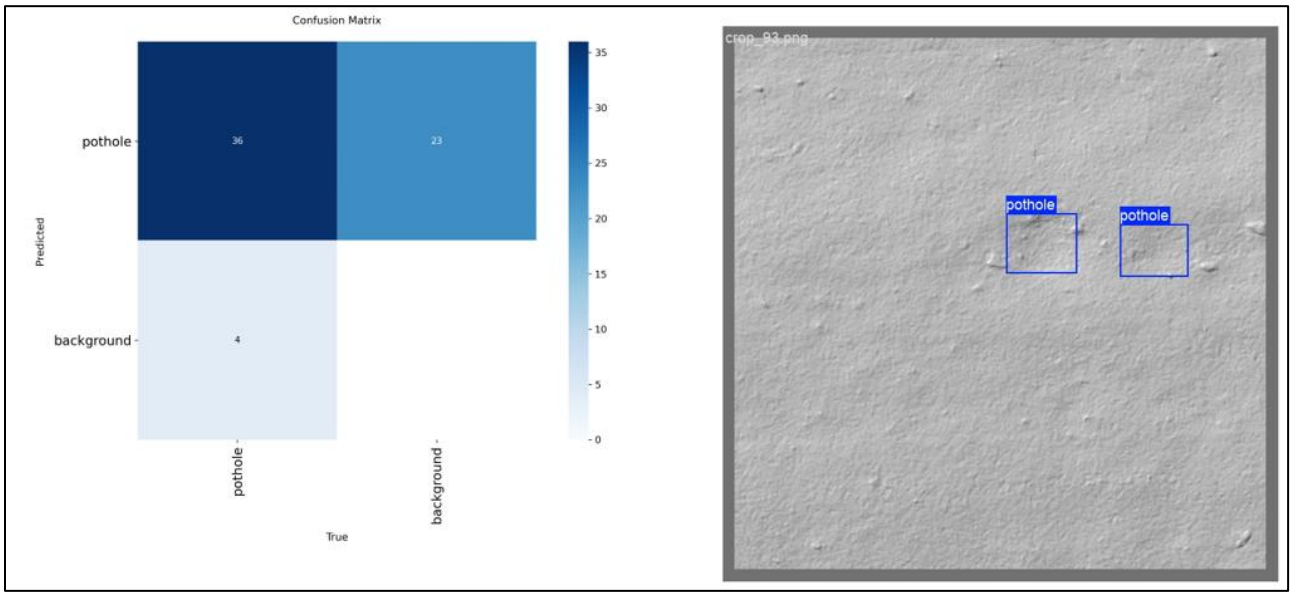

Figure 33. Confusion matrix of Yolov5 performance on validation dataset (left) and sample prediction on validation dataset (right)

The bounded boxes around the potholes were clipped from the DEM data for diameter and depth approximations. Similar to the work done for other distresses, we developed a prototype toolbox in ArcGIS Pro for quick approximation of pothole depth and width. All of the detected potholes are input into the toolbox, and the toolbox assigns each a unique label and determines its severity level. A sample of a detected pothole region is shown in Figure 34, which shows a 3D plot of the pothole.

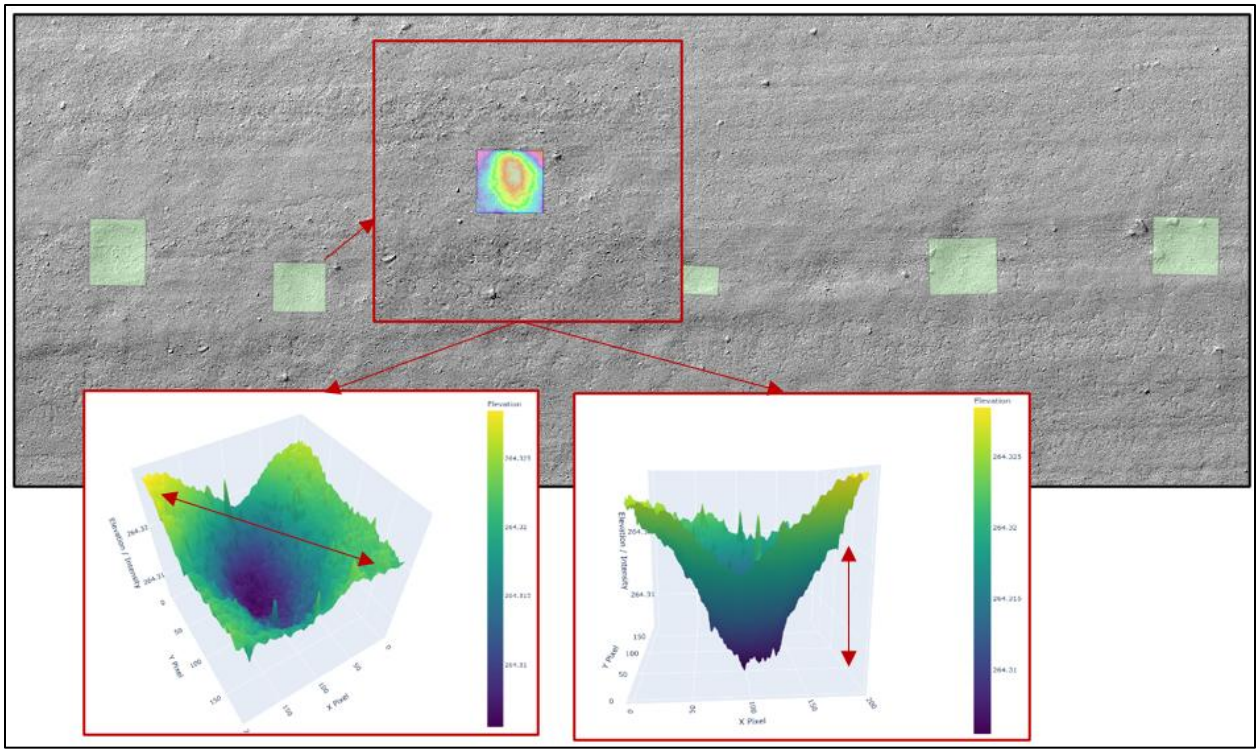

Figure 34. Detected potholes and 3D plots of a sample pothole showing the extent of diameter and depth

Given the high resolution of the DEM data, we compared the depths and diameters of the automatically detected potholes with manually sampled data from foot-on-ground (FOG) observations. Table 8 provides measured DEM and FOG depths and diameters, while Figure 35 and Figure 36 illustrate scatterplots of the FOG and DEM depths and diameters, respectively.

Table 8. Measured pothole depths and diameters from DEM and FOG data

Pothole Number	Depth		Diameter		Severity Match	
	FOG	DEM	FOG	DEM	FOG	DEM
1	1.00	1.04	1.67	2.12	Low*	Med*
2	1.25	1.08	1.33	1.39	Low	Low
3	1.30	1.14	1.67	1.56	Low	Low
4	1.50	1.56	1.75	1.89	Low	Low
5	1.30	1.47	1.67	1.83	Low	Low
6	2.00	1.88	2.42	2.81	High*	Med*
7	1.50	1.57	1.83	1.98	Low	Low
8	1.50	1.48	2.08	2.08	Med	Med
9	4.75	3.93	3.33	3.34	High	High

* Inconsistency between FOG and DEM measurements

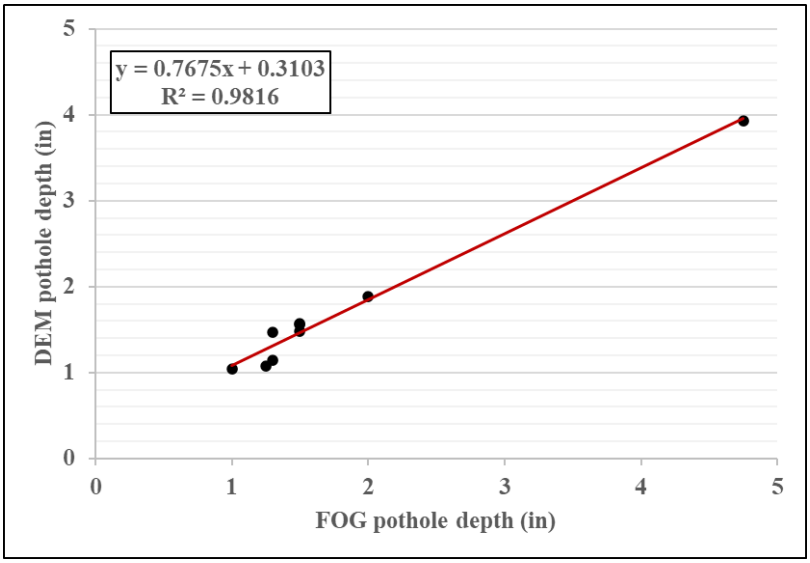

Figure 35. Scatterplot of FOG versus DEM pothole depths with the line of best fit

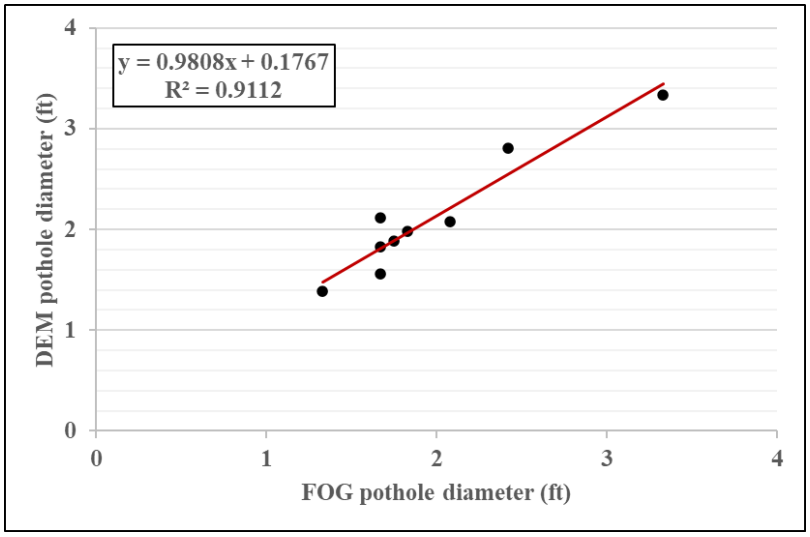

Figure 36. Scatterplot of FOG versus DEM pothole diameters with the line of best fit

As previously stated, the USACE technical manual recommends measuring the total number of potholes for each severity category, implying that accurate automatic measurements of pothole distress severity depend on both the detection of potholes and assessment of their features, e.g., depth and diameter. Following the severity level guidelines in the technical manual, we further categorized each identified pothole by its severity class, providing the additional information given in Table 8. While the automatic DEM-based severity estimation closely aligns with the FOG measurements, the two inconsistent results highlighted in the table differ by only one severity level above or below the FOG measurements.

Loose Aggregate

Loose aggregate is a berm formation typically found in the center of the road or along the less-traveled shoulder. This type of distress was absent at all of the visited sites, making it challenging to validate our proof-of-concept automatic detection toolbox for this distress type. We inferred that the logic used for rut detection would be applicable to loose aggregate detection, but with a distinction in symmetry. While we seek to find ridges and valleys for rut pattern detection, here we seek to find a ridge (berm) between side valleys. We adopted the severity classification provided in the USACE technical manual, categorizing berm heights less than 2 in. as low severity, between 2 and 4 in. as medium severity, and greater than 4 in. as high severity. Similar to the previously discussed elevation-based distresses, we developed a custom ArcGIS Pro toolbox that enables fast and accurate detection of loose aggregate using our algorithmic logic directly applied to DEM data. To align with the USACE technical manual guidelines, which recommend reporting loose aggregate in linear feet per severity, our toolbox generates an HTML report with summarized severities. This report highlights detected berm regions and summarizes the total linear feet of loose aggregate per severity class.

To further improve clarity and measurement precision, we implemented a simplified spatial classification method to distinguish the gravel road center and the less-traveled shoulder, as illustrated in Figure 37, similar to the USACE representation shown in Figure 38. Specifically, the road center is defined as the region within one standard deviation to the left and right of the road's centerline, while the outer edges are designated as areas extending beyond this range, starting at one standard deviation outward. Figure 39 provides screenshots of the parameters required to run the customized toolbox. We have reserved further validation of the developed algorithm for future work.

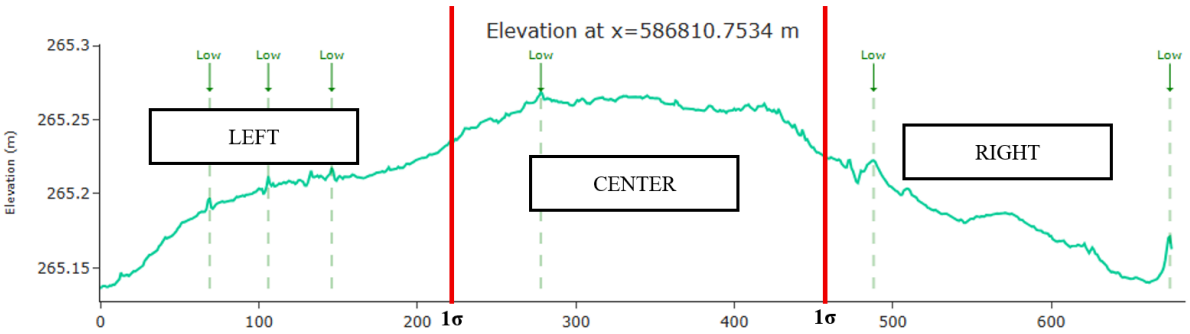

Figure 37. Classification of road section using standard deviation

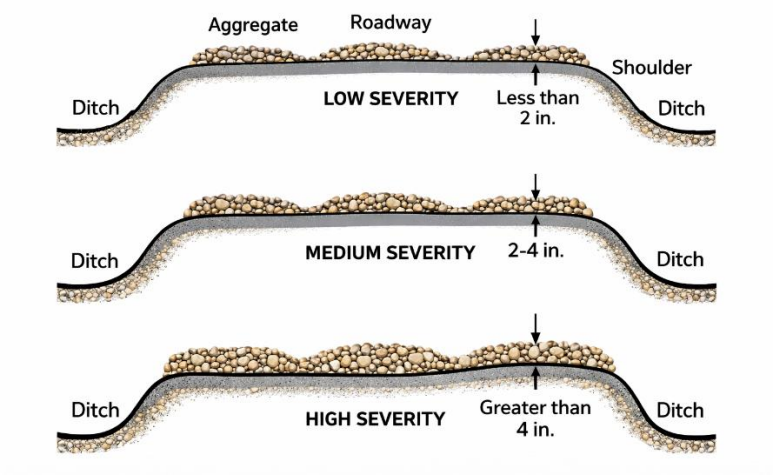

Figure 38. USACE loose aggregate severity classification

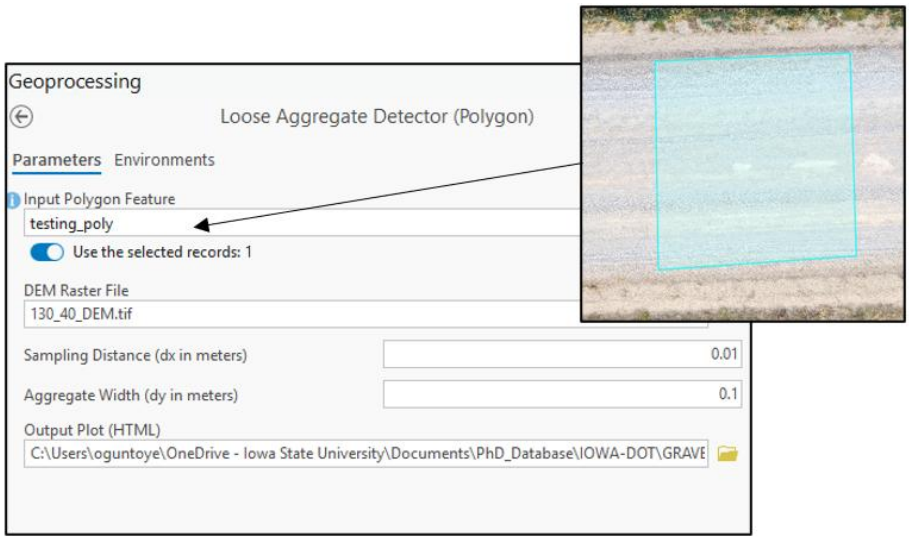

Figure 39. ArcGIS Pro proof-of-concept loose aggregate detection toolbox

Improper Cross-Section (Crown)

A roadway's crown is a key feature that characterizes how a pavement drains water. Crown-related distress includes slope flatness or any impeding feature that causes water to pond, pushing the cross-section away from an expected and ideal condition. While the USACE technical guidelines categorize crown distress on unsurfaced pavement into different severity levels based on slope and the presence of ponding water and depressions, as shown in Figure 40, we developed our final severity classification using a slope and rut feature matrix. Automating the detection of these features demanded setting up some rules. We first identified a slope threshold sufficient to properly drain water. According to Skorseth (2000), a crown slope of approximately 4% is recommended from the pavement edge to the centerline. Although it does not express the preferred crown shape in terms of slope percentage, the PASER manual by the University of Wisconsin–Madison indicates the expected rise between the crown and the road

edges for gravel roads, without reference to a standard width. Given that percentage values are global for any gravel road width, we adopted the Skorseth (2000) standard for our severity matrix, although a higher slope may be expected at banking curve sections.

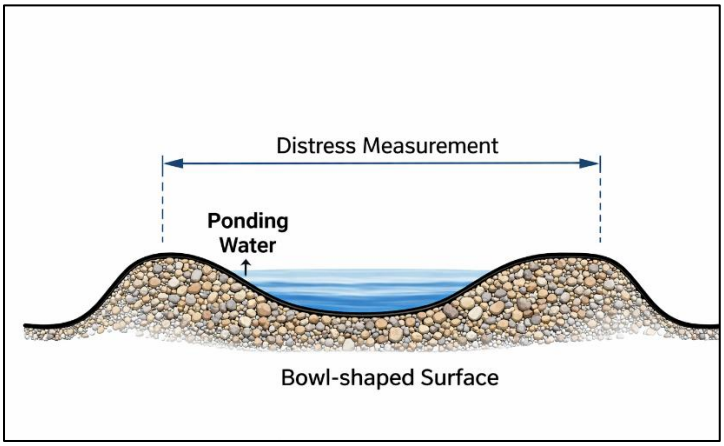

Figure 40. Improper cross-section schematic illustration

Intuitively, V-shaped pavement sections characterized by opposing slopes from the edge to the centerline and from the centerline to the opposite edge (−ve/+ve) were automatically classified as exhibiting high-severity crown distress, even when no rutting or depressions were observed in either lane, and were excluded from further analysis. For example, when a section was identified as nearly flat ($0 \leq x \leq 2$), it was classified as having medium-severity crown distress even when no rutting was present. Other crown severity levels were determined based on the severity matrix presented in Table 9. In general, sections with higher cross-slope values and minimal rutting corresponded to low or no crown distress ratings, whereas reductions in slope or increases in rutting severity resulted in higher crown distress ratings. While this severity matrix served as a guide for our proof-of-concept algorithm, the severities therein may be adapted and/or refined to best suit the use case in industry applications.

Table 9. Developed improper cross-section severity matrix

Slope		Rutting			
Start Edge → Centerline // Centerline → End Edge	**Absolute Average Slope**	**None**	**Low**	**Medium**	**High**
{+ ve // - ve, - ve // - ve, + ve // + ve}	> 6	-	-	Low	Medium
	$4 < x \leq 6$	-	Low	Medium	High
	$2 < x \leq 4$	Low	Medium	High	High
	$0 \leq x \leq 2$	Medium	High	High	High
{-ve / +ve}	-	High	High	High	High

While manually categorizing the severity and length of crown distress along an entire road is laborious, we automated the entire task using DEM-generated data. In an attempt to compare the cross-profiles generated from DEM data with manually sampled points in the field, we manually collected four section points on each gravel road where testing was conducted. During the

manual measurement, two team members on either road edge held onto a rope, while another team member took measurements from the rope level down to the gravel road surface. In this approach, we relied on visually inspecting the rope to ensure that it was straight, a method that may not provide the most accurate data. Since the passage of public traffic over the road after manual measurement and before sUAS data collection could potentially alter the level of achievable accuracy in a comparison of data, we sampled various neighboring fictitious lines close to the lines we manually sampled, running from one edge to the other, then plotted the means and standard deviations of the elevations. We then overlaid the points sampled at 5 and 10 ft on the same plots from both edges to the centerline. Figure 41 provides the derived plots, showing four manually sampled cross-sections and DEM-generated cross-sections.

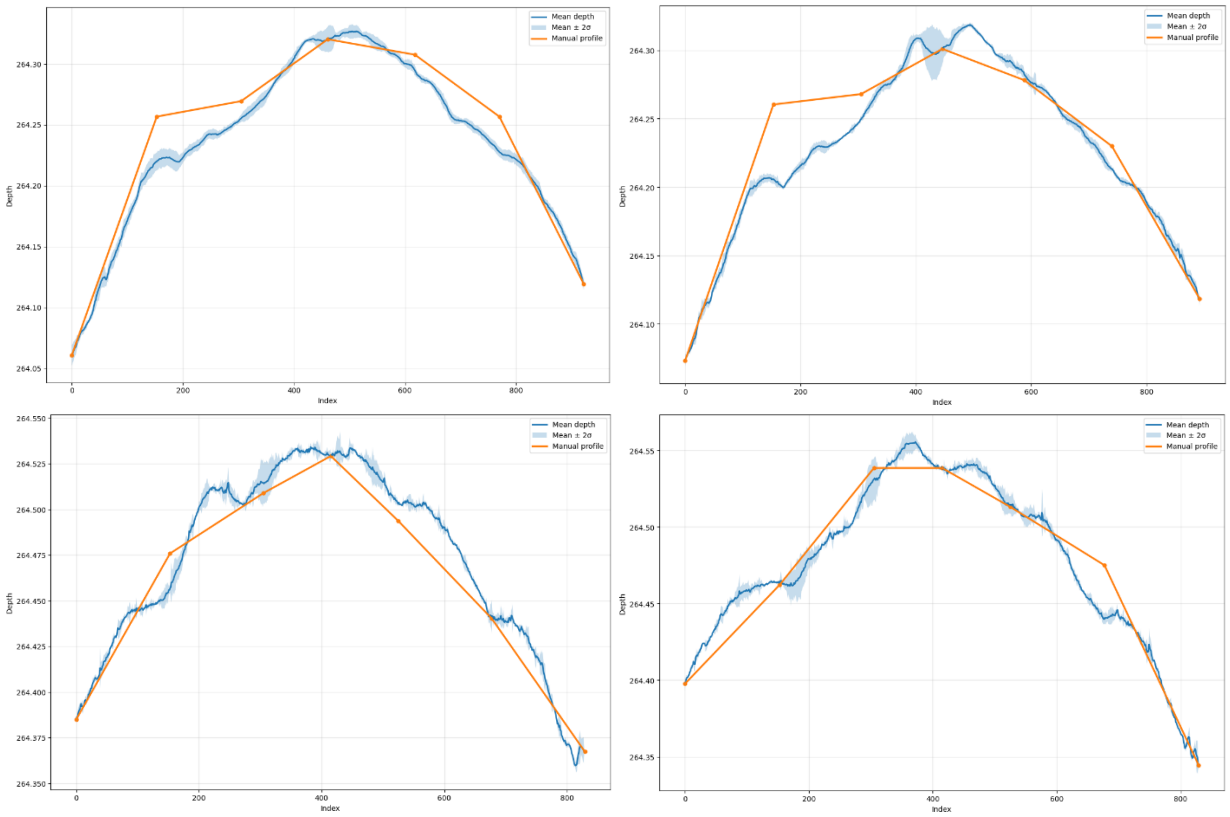

Figure 41. Elevation profiles from DEM data and manual measurements of four sampled cross-sections

Our proof-of-concept crown detection algorithm leveraged the already-developed rut detection algorithm to determine the presence and severity of ruts on each fictitious line running from one edge of the gravel road to the other, and the algorithm further approximated the slope of each lane with respect to the centerline to evaluate the level of cross-section distress severity using the guide in Table 9.

We developed a proof-of-concept toolbox in ArcGIS Pro for the rapid implementation of our algorithms and for performance testing. The final outputs of the program provide the linear feet of each severity class to estimate the deduct values recommended in the USACE technical

manual. We tested the algorithm for the two sites: 150th Street and 130th Street in Buchanan County, Iowa. Figure 42 and Figure 43 show the resulting reports for the two site sections, with the orthophoto of each selected section shown in the inset. While we set the spacing between the fictitious vertical line in the polygon to 0.65 ft (0.2 m), the DEM data points were sampled on each line at a constant frequency of 10 per 100 pixels. As noted in Figure 42, medium- and low-severity ruts were detected on the crown lines, resulting in the final crown severity based on the calculated slope and the formulated matrix in Table 9. As illustrated in Figure 43, the consistently high rut severity along the frost boil regions, combined with the estimated average slope index, resulted in an increase in the crown severity in the summarized report. It is essential to note that a more refined result would be achieved if the spacing between the fictitious lines were reduced, allowing the algorithm to limit the assumption of continued distress feature characteristics for each fictitious line within the polygon.

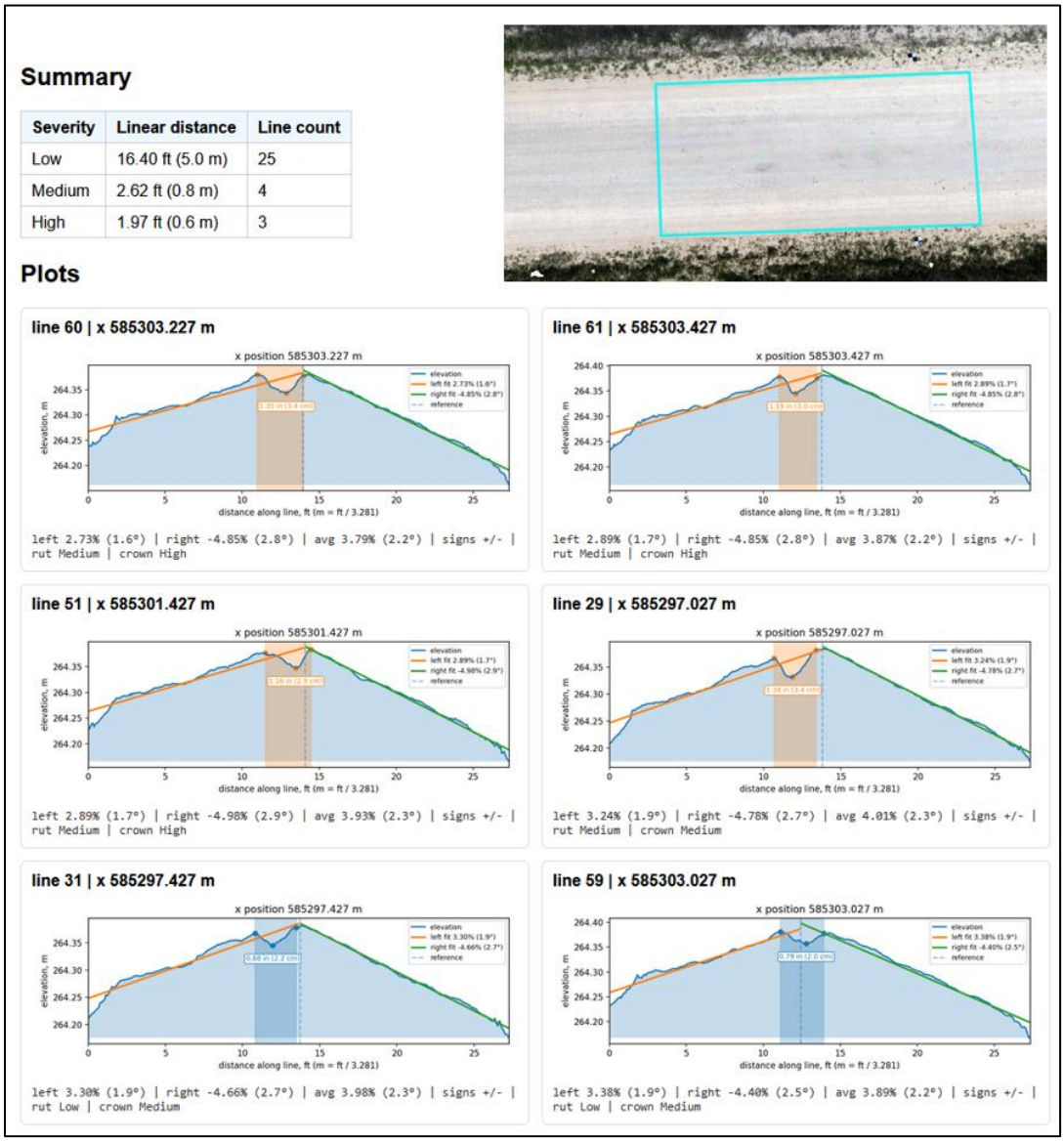

Figure 42. Crown distress report for a section on 150th Street

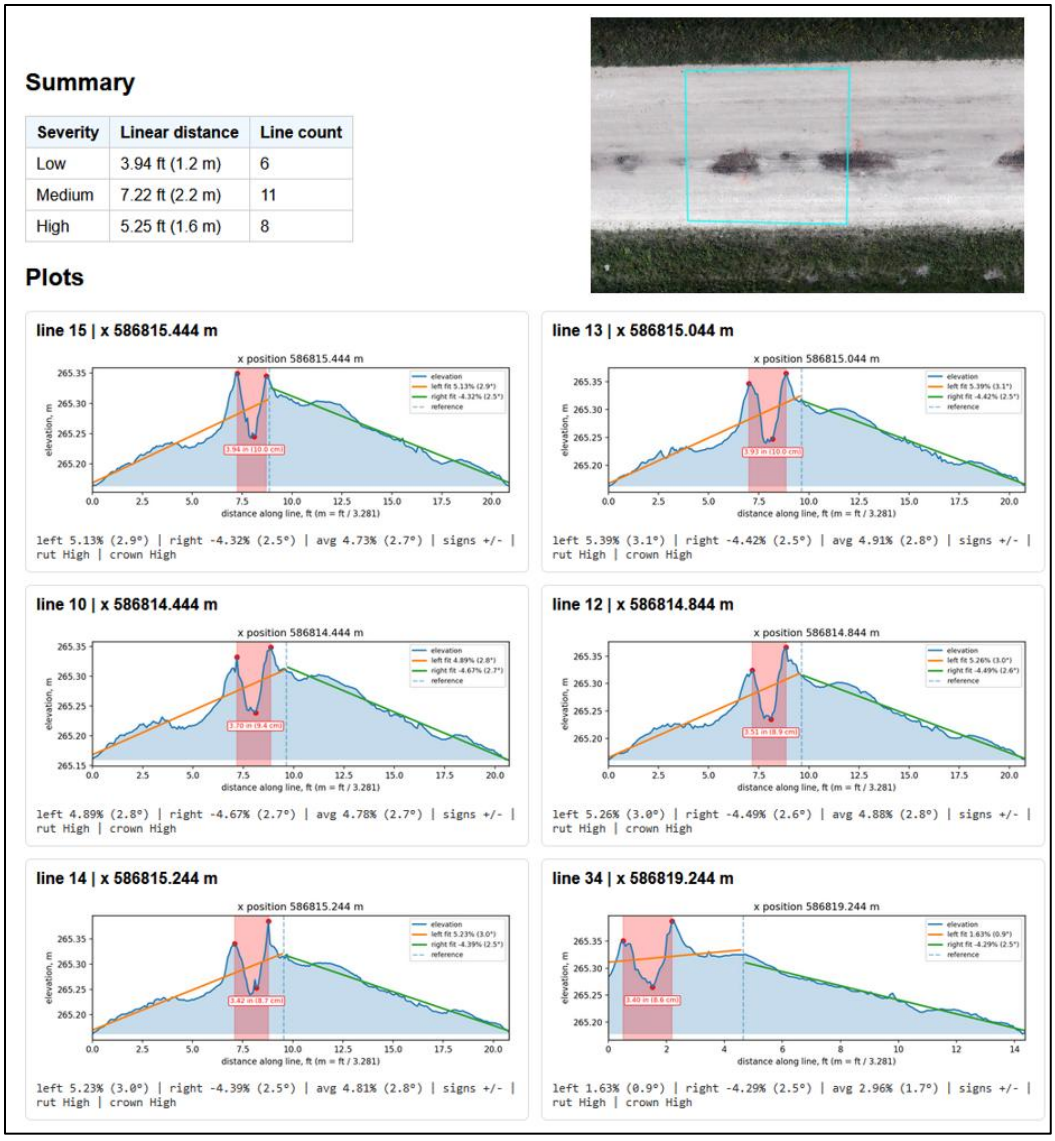

Figure 43. Crown distress report for a section on 130th Street

We added a visual feature that provides a quick overview of crown distress across an entire bounded sample unit. As shown in Figure 44, the developed proof-of-concept toolbox can add a polygonal heatmap explicitly showing regions where crown distress has been detected and the severity level of this distress. This visualization helps users make quick judgments about a gravel road section's ability to effectively drain water and the section of the road that needs intervention.

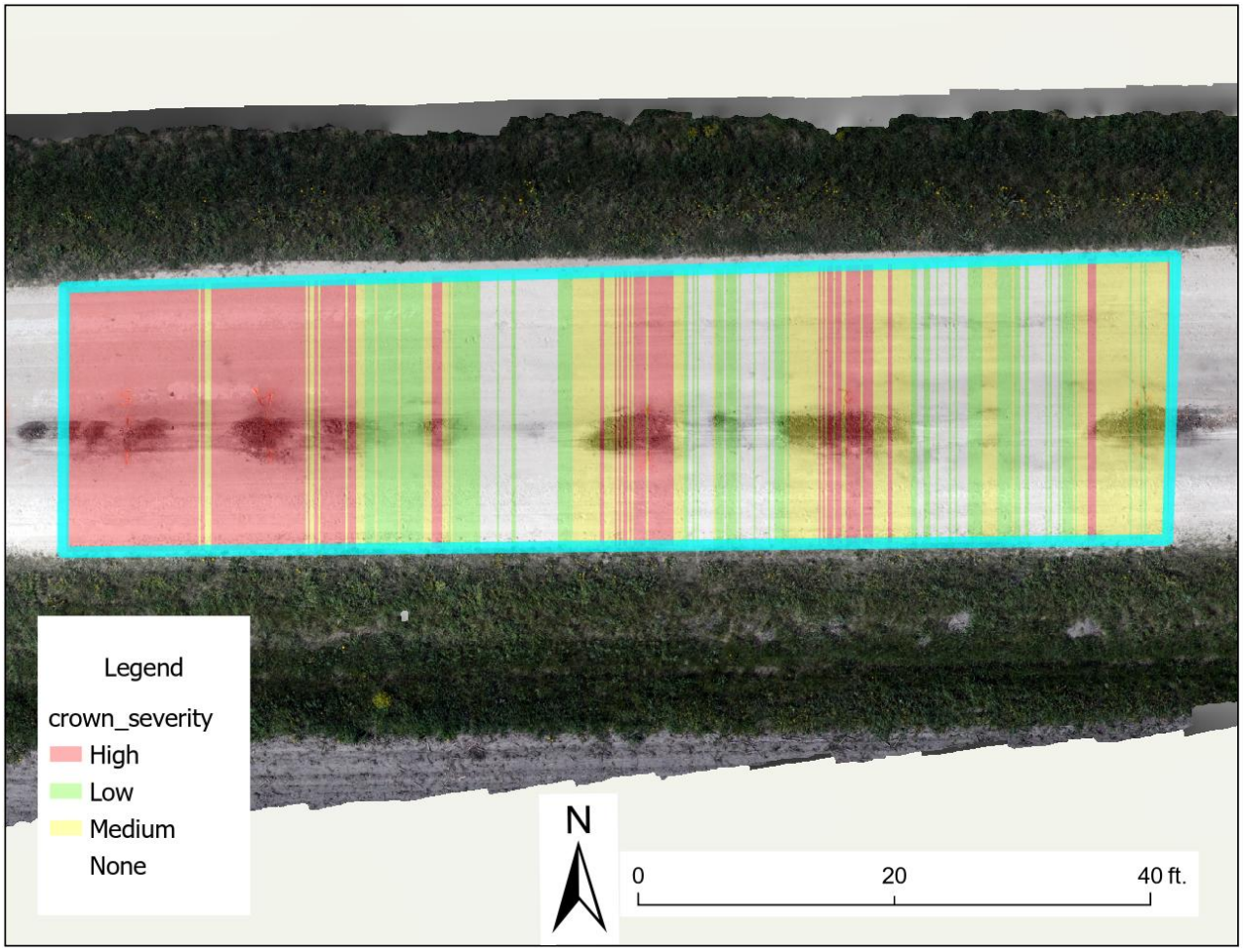

Figure 44. Screenshot of heatmap result for crown distress detection

PROOF-OF-CONCEPT WEB APPLICATION

As described in the previous chapter, automatic distress identification and quantification algorithms were created for each type of gravel road distress. While ArcGIS Pro software provides seamless integration of programming scripts through toolbox customization, it is challenging to share the scripts with non-ArcGIS Pro users, since they will be required to install programming packages and navigate other programmatic hurdles. It is also currently challenging to upload video data to the software for extracting dust cloud severity levels from the recorded sUAS videos. Because of these bottlenecks, we explored the feasibility of utilizing a web application as a single-spot, easy-to-use platform for all distress quantification. In this section, we share progress on developing a web application that ingests processed sUAS data and performs rut analysis using the developed rut toolbox.

Step A: User Registration

New users must register and log in as shown in Figure 45 and Figure 46.

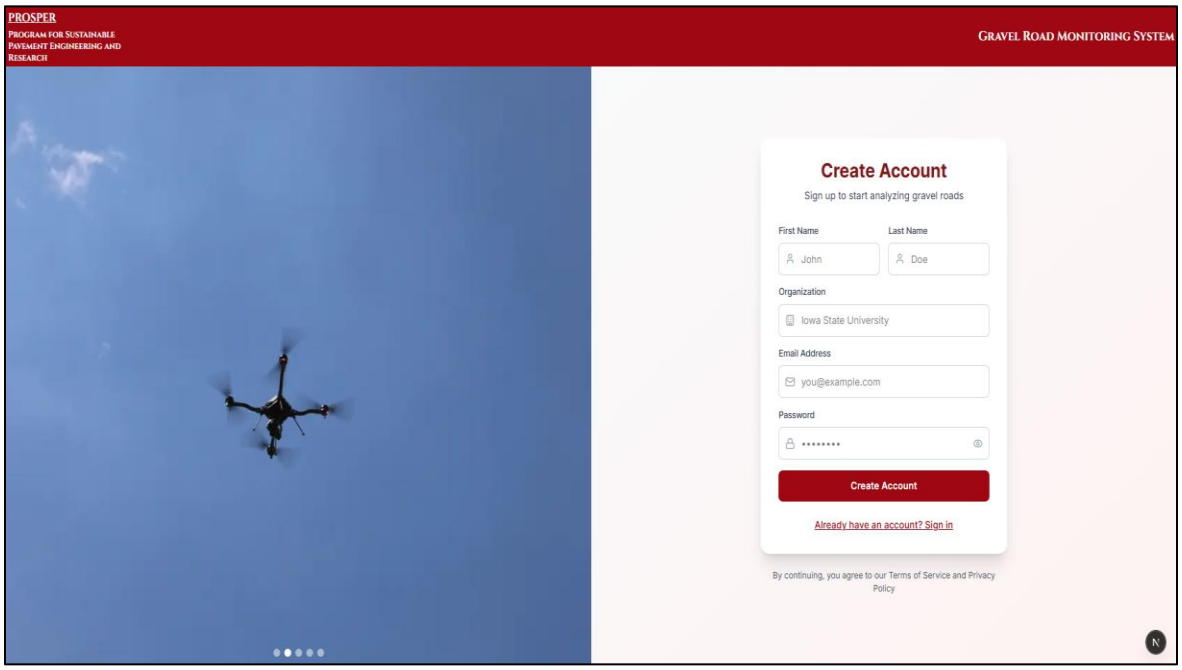

Figure 45. Sign-up page for new users

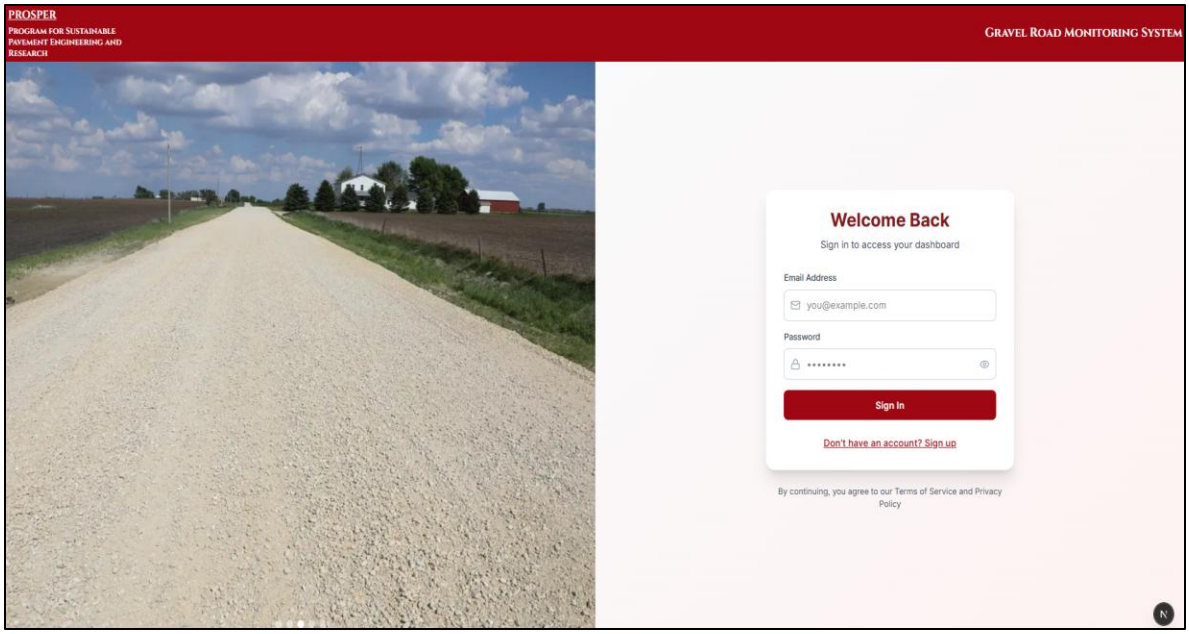

Figure 46. Login page for registered users

Step B: Data Upload

Logged-in users have access to the dashboard and the rut feature detection tool. To begin the analysis, users are expected to upload files such as DEMs and orthophotos, as shown in Figure 47.

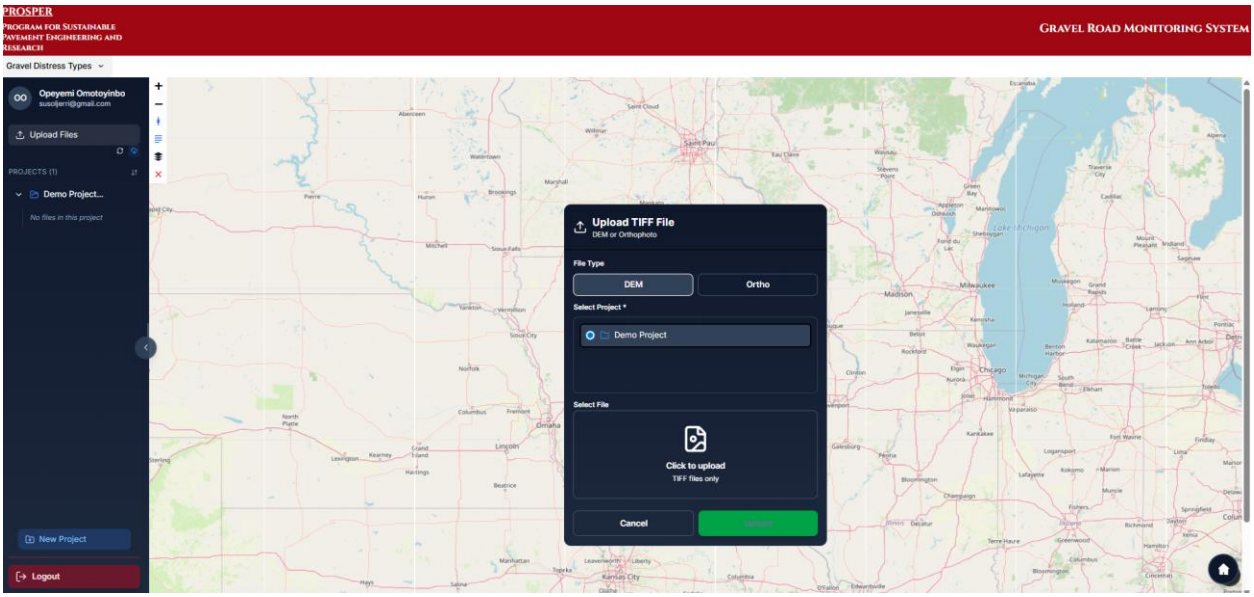

Figure 47. Interface for uploading processed sUAS data into the project folder

Step C: Analysis

When a user uploads data, background processes begin tiling the uploaded DEM and orthophoto TIFF files into smaller images, which are then forwarded to a content delivery database to enable quick navigation when the images are viewed. Figure 48 shows the uploaded files under the project name 130th Street, with the overlaid hillshade image selected for viewing. Using the provided drawing tools, users can also draw a bounded polygon over a DEM, orthophoto, or hillshade model to identify a region of interest. Figure 49 shows a bounded region of the 130th Street hillshade model, along with a complete rut analysis for the bounded region. The analysis form is similar to the one presented earlier in the discussion on rutting analysis, and the results can be viewed interactively and in PDF format, in which users can see the approximated deduct values that the program has automatically generated by calculating the density of each distress category with respect to the overall bounded region. The USACE technical manual provides plots for calculating deduct values for every distress, and we extracted the plotted values and integrated them into our system for automatic approximations, as shown in Figure 50.

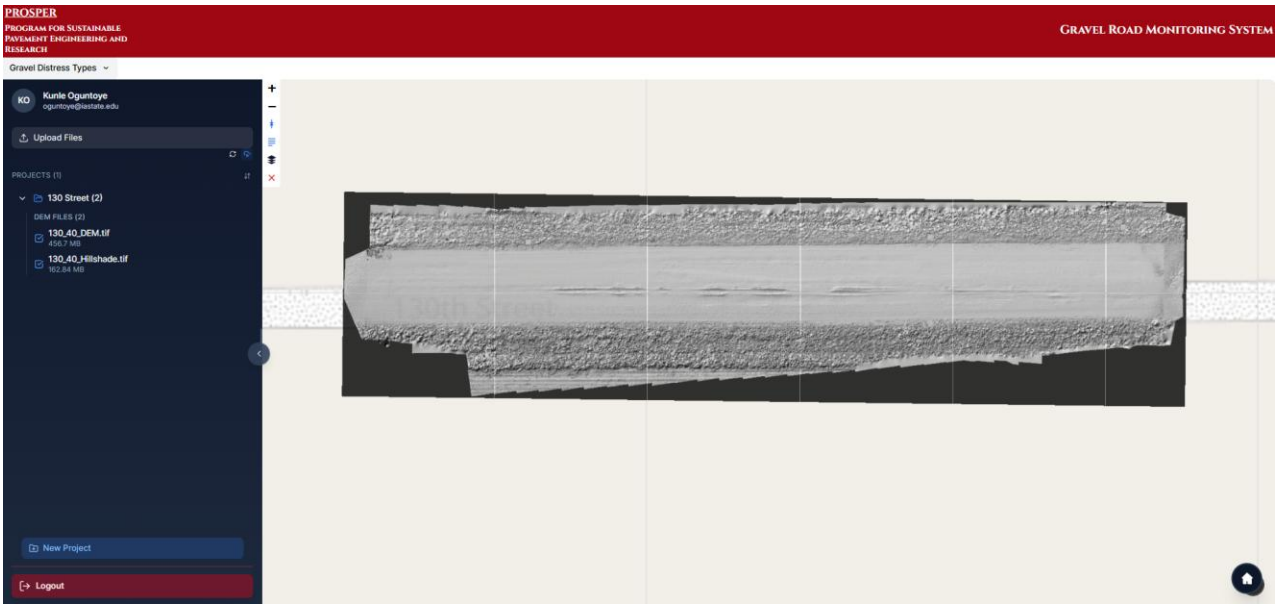

Figure 48. Quick view and navigation interface after successful background tiling of uploaded DEM and orthophotos

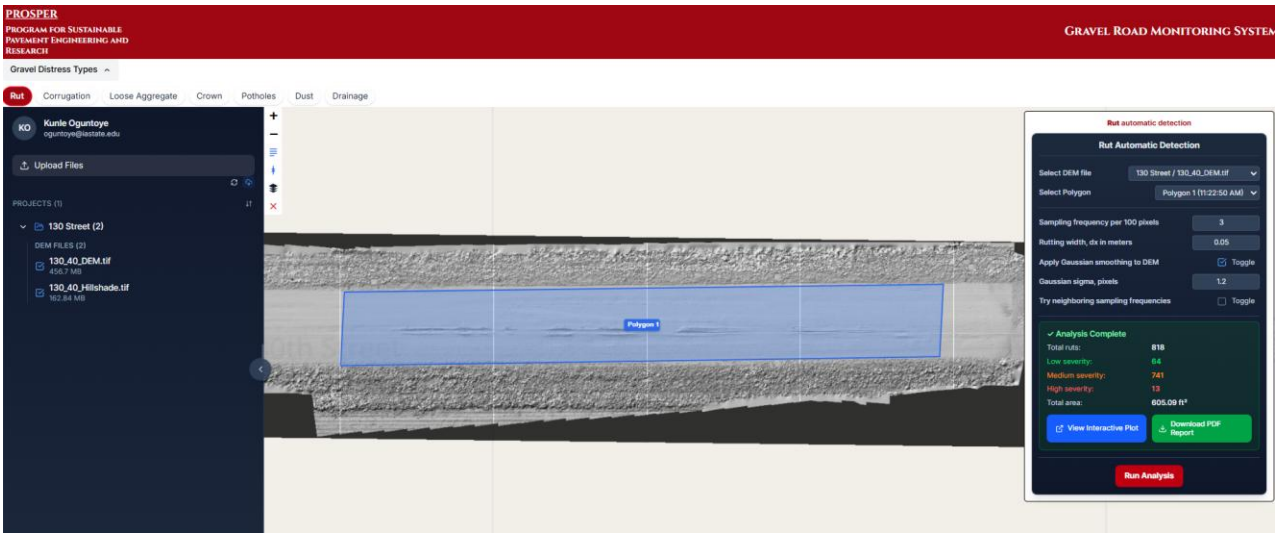

Figure 49. Bounded region and completed rut analysis with options to download PDF report and view interactive HTML output

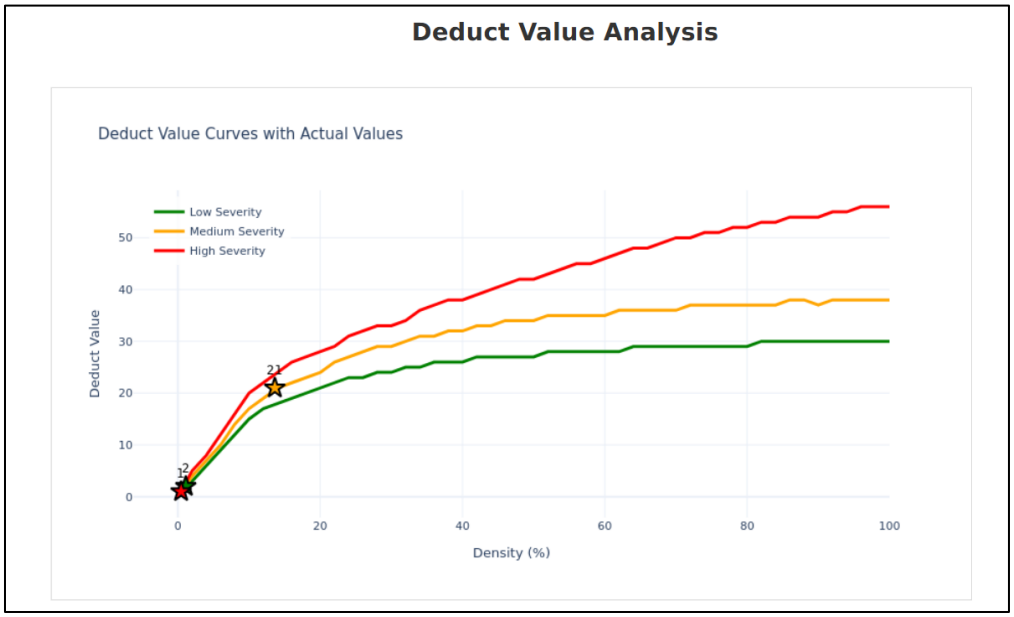

Figure 50. Automatic approximation of the deduct value per severity class

SUMMARY/CONCLUSION

This study, building upon previous work by Michigan Technological University team members, investigated the application of sUAS in monitoring gravel roads. Traditional manual inspection of gravel roads is laborious, time-consuming, and very subjective. The use of sUAS presents a significant opportunity to rapidly collect data critical for extracting gravel road features. The majority of distresses associated with gravel roads—such as rutting, potholes, corrugation, loose aggregate, and improper crown—are depth based, and DEM data are critical for analysis. Methods to detect these depth-based distresses share a similar data collection scope, as the sUAS is flown at a predefined altitude, with the sensor camera facing downward orthogonally. Other distresses that can be assessed through image-based analysis include excessive dust and improper drainage. We focused on assessing dust severity using sUAS video recordings and used deep learning models to quantify dust cloud severity in each video frame. Lastly, we reserved analysis of drainage for manual visual assessment, in which reviewers determine the degree of ponding or debris-caused impediments to water flow. Through comparisons with manually measured points, we validated our proof-of-concept algorithms for automatically and semiautomatically extracting distress features. This sUAS-enabled remote-sensing project showed potential benefits in terms of accurate approximation of gravel road conditions. This benefit can help counties perform necessary maintenance activities on time and better manage their transportation infrastructure.

We developed proof-of-concept toolboxes for distress quantification, which have shown promising results in detecting and quantifying distress severities from processed sUAS data, such as DEMs and orthophotos. Key findings were as follows:

- The estimated time needed for sUAS data collection and processing depends on different factors, such as flight altitude, the characteristics of the gravel road section, and the computation resources available for image processing.
- The rutting tool measured slightly lower rutting values than those obtained through manual measurement but classified the observed rutting in the same severity levels. However, detecting and rating low-severity rutting remains challenging, and more data points are needed to further validate the prototype algorithm.
- The corrugation detection tool achieved an R^2 value of 0.74 when its results were compared the ground truth data. We anticipate a higher correlation in a more ideal scenario, free of moving traffic during data collection.
- The trained deep learning model (ResNet152) was able to categorize dust severity into No Dust, Low Dust, and High Dust with an F1 score of 0.95 on test dataset predictions.
- The results from the pothole detection toolbox closely matched those of FOG measurements in terms of depth and width, with an R^2 of 0.98 for depth and an R^2 of 0.91 for width.
- The loose aggregate prototype toolbox requires additional field measurements to validate and further refine the detection algorithm.
- An improper cross-section severity matrix was proposed, and the generated profile from the toolbox closely aligned with manually measured profile points.
- A DEM resolution of 1.5 mm or better improves the precision of distress quantification.

- The limited availability of large datasets, due to the urgent need for rapid maintenance interventions, restricts comprehensive validation of the proof-of-concept algorithms developed in this study.
- The single-stop web application developed as part of this research enables users to assess rutting distress severity from gravel road datasets.

The major limitations of this study were as follows:

- Insufficient datasets were available to fully validate the developed proof-of-concept distress detection toolboxes due to frequent grading activities on gravel roads. For instance, the rut detection algorithm was validated using only 3 manually sampled points, the corrugation detection algorithm was validated using 20 points, and the pothole detection algorithm was validated using 9 points. Similarly, the visited sites predominantly exhibited extreme dust conditions, either low or high, which limited the availability of training data for medium-severity dust levels as prescribed in the USACE technical manual.
- Drainage assessment was conducted manually because many drainage structures are located near overhead power lines, areas that the sUAS is programmed to avoid for safety reasons.

We aim to further extend our work in future research projects by conducting the following tasks:

- Visit additional gravel road sites and collect more sUAS data to improve the developed pattern recognition algorithms.
- Identify and visit additional gravel road sites with varying levels of loose aggregate distress to validate the developed algorithms for this distress type.
- Develop a framework for drainage condition rating, since the severity of drainage-related distress also contributes to the overall deduct values needed to estimate a gravel road's URCI.
- Refine, train, validate, and containerize the proof-of-concept toolboxes for the Iowa DOT.
- Continue to enhance the comprehensive and robust single-stop web applications where users can upload their sUAS-collected data and perform distress analysis.

REFERENCES

Aela, P., H.-L. Chi, A. Fares, T. Zayed, and M. Kim. 2024. UAV-based studies in railway infrastructure monitoring. *Automation in Construction*, Vol. 167, 105714. https://doi.org/10.1016/j.autcon.2024.105714.

Alzubaidi, H., and R. Magnusson. 2002. Deterioration and rating of gravel roads: State of the art. *Road Materials and Pavement Design*, Vol. 3, No. 3, pp. 235–260. https://doi.org/10.1080/14680629.2002.9689924.

Banić, M., A. Miltenović, M. Pavlović, and I. Ćirić. 2019. Intelligent machine vision based railway infrastructure inspection and monitoring using UAV. *Facta Universitatis, Series: Mechanical Engineering*, Vol. 17, No. 3, pp. 357–364. https://doi.org/10.22190/FUME190507041B.

Biçici, S., and M. Zeybek. 2021. An approach for the automated extraction of road surface distress from a UAV-derived point cloud. *Automation in Construction*, Vol. 122, 103475. https://doi.org/10.1016/j.autcon.2020.103475.

Bosurgi, G., M. Modica, O. Pellegrino, and G. Sollazzo. 2023. An automatic pothole detection algorithm using pavement 3D data. *International Journal of Pavement Engineering*, Vol. 24, No. 2, 2057978. https://doi.org/10.1080/10298436.2022.2057978.

Breitenbach, S. 2017. Dirt roads help some cities, counties drive down costs. *Stateline*, January 17, 2017. https://stateline.org/2017/01/17/dirt-roads-help-some-cities-counties-drive-down-costs/.

Brooks, C., R. J. Dobson, D. M. Banach, C. Roussi, V. Lefler, B. Hart, J. Garbarino, A. Lawrence, B. White, S. Aden, and T. K. Colling. 2016. *Characterization of Unpaved Road Condition through the Use of Remote Sensing Project – Phase II; Deliverable 8-D: Final Report*. Michigan Tech Transportation Institute. https://rosap.ntl.bts.gov/view/dot/32118.

Bučko, B., E. Lieskovská, K. Zábovská, and M. Zábovský. 2022. Computer vision based pothole detection under challenging conditions. *Sensors*, Vol. 22, No. 22, 8878. https://doi.org/10.3390/s22228878.

Dobson, R. J., C. Brooks, C. Roussi, and T. Colling. 2013. Developing an unpaved road assessment system for practical deployment with high-resolution optical data collection using a helicopter UAV. *2013 International Conference on Unmanned Aircraft Systems*, pp. 235–243. IEEE.

Dobson, R. J., T. Colling, C. Brooks, C. Roussi, M. K. Watkins, and D. Dean. 2014. Collecting decision support system data through remote sensing of unpaved roads. *Transportation Research Record*, Vol. 2433, No. 1, pp. 108–115. https://doi.org/10.3141/2433-12.

Eaton, R. A., and R. E. Beaucham. 1992. *Unsurfaced Road Maintenance Management*. Special Report 92-26. U.S. Army Corps of Engineers, Cold Regions Research & Engineering Laboratory.

Fischer, S., E. Lawless, J. Lu, and K. Van Fossen. 2020. *Global Benchmarking Study on Unmanned Aerial Systems for Surface Transportation: Domestic Desk Review*. Federal Highway Administration. https://www.fhwa.dot.gov/uas/hif20091.pdf.

Flammini, F., C. Pragliola, and G. Smarra. 2016. Railway infrastructure monitoring by drones. International Conference on Electrical Systems for Aircraft, Railway, Ship Propulsion and Road Vehicles and International Transportation Electrification Conference (ESARS-ITEC), November 2–4, Toulouse, France.

He, K., X. Zhang, S. Ren, and J. Sun. 2015. Deep residual learning for image recognition. *arXiv*: 1512.03385. https://arxiv.org/abs/1512.03385.
Hubbard, S., A. Pak, Y. Gu, and Y. Jin. 2017. UAS to support airport safety and operations: Opportunities and challenges. *Journal of Unmanned Vehicle Systems*, Vol. 6, No. 1, pp. 1–17. https://doi.org/10.1139/juvs-2016-0020.
Huntington, G., and K. Ksaibati. 2015. Visual assessment system for rating unsealed roads. *Transportation Research Record*, Vol. 2474, No. 1, pp. 116–122. https://doi.org/10.3141/2474-14.
ICEA. n.d. About Secondary Roads. Iowa County Engineers Association. https://www.iowacountyroads.org/about-secondary-roads.
InTrans. 2021. Iowa Granular Road Structural Design Tool. Institute for Transportation, Iowa State University. https://www.intrans.iastate.edu/research/in-progress/iowa-granular-road-structural-design-tool/.
Khilji, T. N., L. Lopes Amaral Loures, and E. R. Azar. 2021. Distress recognition in unpaved roads using unmanned aerial systems and deep learning segmentation. *Journal of Computing in Civil Engineering*, Vol. 35, No. 2, 04020061. https://doi.org/10.1061/(ASCE)CP.1943-5487.0000952.
Label Studio. n.d. Open Source Data Labeling and AI Evaluation. Label Studio. https://labelstud.io/.
Lopes Amaral Loures, L., and E. R. Azar. 2023. Condition assessment of unpaved roads using low-cost computer vision–based solutions. *Journal of Transportation Engineering, Part B: Pavements*, Vol. 149, No. 1, 04022066. https://doi.org/10.1061/JPEODX.PVENG-1006.
Ma, N., J. Fan, W. Wang, J. Wu, Y. Jiang, L. Xie, and R. Fan. 2022. Computer vision for road imaging and pothole detection: A state-of-the-art review of systems and algorithms. *Transportation Safety and Environment*, Vol. 4, No. 4, tdac026. https://doi.org/10.1093/tse/tdac026.
McGuire, M., M. J. Rys, and A. Rys. 2016. *A Study of How Unmanned Aircraft Systems Can Support the Kansas Department of Transportation's Efforts to Improve Efficiency, Safety, and Cost Reduction*. Report No. K-TRAN: KSU-15-3. Kansas Department of Transportation, Topeka, KS.
Mitra, R., M. A. A. Sourav, S. Kim, B. Gulmezoglu, and H. Ceylan. 2025. Comparative case study: Traffic monitoring using YOLOv11-based object detection and two tracking algorithms with small uncrewed aerial systems. International Conference on Transportation and Development 2025, pp. 311–321. American Society of Civil Engineers. https://doi.org/10.1061/9780784486191.027.
Nooralishahi, P., C. Ibarra-Castanedo, S. Deane, F. López, S. Pant, M. Genest, N. P. Avdelidis, and X. P. V. Maldague. 2021. Drone-based non-destructive inspection of industrial sites: A review and case studies. *Drones*, Vol. 5, No. 4, pp. 106. https://doi.org/10.3390/drones5040106.
Oguntoye, K. S., S. Laflamme, R. Sturgill, and D. J. Eisenmann. 2023. Review of artificial intelligence applications for virtual sensing of underground utilities. *Sensors*, Vol. 23, No. 9, 4367. https://doi.org/10.3390/s23094367.

Oguntoye, K. S., M. A. A. Sourav, R. Mitra, A. Jenkins, H. Ceylan, S. Kim, B. Gulmezoglu, Y. Mo, and C. Brooks. 2025. Low-altitude sUAS flights for remote sensing of submillimeter hairline cracks: A case study. International Conference on Transportation and Development 2025, pp. 800–809. American Society of Civil Engineers. https://doi.org/10.1061/9780784486191.070.

Pietersen, R. A., M. S. Beauregard, and H. H. Einstein. 2022. Automated method for airfield pavement condition index evaluations. *Automation in Construction*, Vol. 141. https://doi.org/10.1016/J.AUTCON.2022.104408.

Sattar, S., S. Li, and M. Chapman. 2018. Road surface monitoring using smartphone sensors: A review. *Sensors*, Vol. 18, No. 11. https://doi.org/10.3390/s18113845.

Skorseth, K. 2000. *Gravel Roads: Maintenance and Design Manual*. Federal Highway Administration.

Sourav, M. A. A., H. Ceylan, C. Brooks, R. Dobson, S. Kim, D. Peshkin, and M. Brynick. 2024. Use of small unmanned aircraft systems in airfield pavement inspection: Implementation and potential. *International Journal of Pavement Engineering*, Vol. 25, No. 1. https://doi.org/10.1080/10298436.2024.2401630.

Sourav, M. A. A., H. Ceylan, C. Brooks, D. Peshkin, S. Kim, R. Dobson, C. Cook, M. Mahedi, and A. Jenkins. 2023a. *Small Unmanned Aircraft System for Pavement Inspection*. DOT/FAA/TC-23/50. Federal Aviation Administration.

Sourav, M. A. A., H. Ceylan, S. Kim, C. Brooks, D. Peshkin, R. Dobson, and M. Brynick. 2023b. Use of digital elevation model for detecting airfield pavement distress. *Airfield and Highway Pavements 2023*, pp. 254–265. American Society of Civil Engineers. https://doi.org/10.1061/9780784484906.024.

Sourav, M. A. A., H. Ceylan, S. Kim, C. Brooks, D. Peshkin, R. Dobson, M. Brynick, and M. DiPilato. 2022. Small uncrewed aircraft systems-based orthophoto and digital elevation model creation and accuracy evaluation for airfield portland cement concrete pavement distress detection and rating. *International Conference on Transportation and Development 2022*, pp. 168–180. American Society of Civil Engineers. https://doi.org/10.1061/9780784484371.016.

Sourav, M. A. A., M. Mahedi, H. Ceylan, S. Kim, C. Brooks, D. Peshkin, R. Dobson, and M. Brynick. 2023c. Evaluation of small uncrewed aircraft systems data in airfield pavement crack detection and rating. *Transportation Research Record*, Vol. 2677, No. 1, pp. 653–668. https://doi.org/10.1177/03611981221101030.

Tan, Y., and Y. Li. 2019. UAV photogrammetry-based 3D road distress detection. *ISPRS International Journal of Geo-Information*, Vol. 8, No. 9, p. 409. https://doi.org/10.3390/ijgi8090409.

Vidyadharan, A., T. Carter, H. Ceylan, C. Bloebaum, K. Gopalakrishnan, and S. Kim. 2017. Civil infrastructure health monitoring and management using unmanned aerial systems. *Airfield and Highway Pavements 2017*, pp. 207–216. American Society of Civil Engineers. https://doi.org/10.1061/9780784480946.019.

Watts, A. C., V. G. Ambrosia, and E. A. Hinkley. 2012. Unmanned aircraft systems in remote sensing and scientific research: Classification and considerations of use. *Remote Sensing*, Vol. 4, No. 6, pp. 1671–1692. https://doi.org/10.3390/rs4061671.

Zeybek, M., and S. Biçici. 2020. Road Distress Measurements Using UAV. *Turkish Journal of Remote Sensing and GIS*, Vol. 1, No. 1, pp. 13–23.

Zhang, C. 2008. An UAV-based photogrammetric mapping system for road condition assessment. *The International Archives of the Photogrammetry, Remote Sensing and Spatial Information Sciences*, Vol. XXXVII, Part B5. International Society for Photogrammetry and Remote Sensing.

THE INSTITUTE FOR TRANSPORTATION IS THE FOCAL POINT FOR TRANSPORTATION AT IOWA STATE UNIVERSITY.

InTrans centers and programs perform transportation research and provide technology transfer services for government agencies and private companies;

InTrans contributes to Iowa State University and the College of Engineering's educational programs for transportation students and provides K–12 outreach; and

InTrans conducts local, regional, and national transportation services and continuing education programs.

IOWA STATE UNIVERSITY

Visit **InTrans.iastate.edu** for color pdfs of this and other research reports.